HHS Public Access
Author manuscript
Cell Rep. Author manuscript; available in PMC 2021 May 20.

Published in final edited form as:
Cell Rep. 2020 November 10; 33(6): 108362. doi:10.1016/j.celrep.2020.108362.

Prepronociceptin-Expressing Neurons in the Extended Amygdala Encode and Promote Rapid Arousal Responses to Motivationally Salient Stimuli

Jose Rodriguez-Romaguera[#1,2], **Randall L. Ung**[#2,3], **Hiroshi Nomura**[1,2], **James M. Otis**[1,2], **Marcus L. Basiri**[2,3], **Vijay M.K. Namboodiri**[1,2], **Xueqi Zhu**[1,2], **J. Elliott Robinson**[2,3], **Hanna E. van den Munkhof**[1,2], **Jenna A. McHenry**[1,2], **Louisa E.H. Eckman**[1,2], **Oksana Kosyk**[1,2], **Thomas C. Jhou**[4], **Thomas L. Kash**[3,5], **Michael R. Bruchas**[6,8], **Garret D. Stuber**[1,2,3,7,8,10,*]

[1]Department of Psychiatry, University of North Carolina, Chapel Hill, NC 72599, USA

[2]Neuroscience Center, University of North Carolina, Chapel Hill, NC 72599, USA

[3]Neuroscience Curriculum, University of North Carolina, Chapel Hill, NC 72599, USA

[4]Department of Neuroscience, Medical University of South Carolina, Charleston, SC 29425, USA

[5]Bowles Center for Alcohol Studies, Department of Pharmacology, University of North Carolina, Chapel Hill, NC 72599, USA

[6]Department of Anesthesiology, Washington University Pain Center, Department of Neuroscience, Division of Biology & Biomedical Sciences; and Department of Biomedical Engineering, Washington University, St. Louis, MO 63130, USA

[7]Department of Cell Biology and Physiology, University of North Carolina, Chapel Hill, NC 72599, USA

[#] These authors contributed equally to this work.

SUMMARY

Motivational states consist of cognitive, emotional, and physiological components controlled by multiple brain regions. An integral component of this neural circuitry is the bed nucleus of the stria terminalis (BNST). Here, we identify that neurons within BNST that express the gene *prepronociceptin* (*Pnoc*$^{\mathrm{BNST}}$) modulate rapid changes in physiological arousal that occur upon

---

This is an open access article under the CC BY-NC-ND license (http://creativecommons.org/licenses/by-nc-nd/4.0/).

[*]Correspondence: gstuber@uw.edu.
[8]Present address: Center for the Neurobiology of Addiction, Pain, and Emotion, Department of Anesthesiology and Pain Medicine and Department of Pharmacology, University of Washington, Seattle, WA 98195, USA

AUTHOR CONTRIBUTIONS
Conceptualization, J.R.-R., R.L.U., and G.D.S.; Investigation, J.R.-R., M.L.B., J.M.O., H.N., J.E.R., X.Z., H.E.v.d.M., J.A.M., L.E.H.E., and O.K.; Formal Analysis, R.L.U., J.R.-R., M.L.B., J.M.O., V.M.K.N., H.N., and G.D.S.; Resources, T.C.J., T.L.K., and M.R.B.; Writing – Original Draft, J.R.-R., R.L.U., and G.D.S., Writing – Review & Editing, J.R.-R., R.L.U., and G.D.S.; Fund Acquisition, G.D.S.; Supervision, G.D.S.
[10]Lead Contact

SUPPLEMENTAL INFORMATION
Supplemental Information can be found online at https://doi.org/10.1016/j. celrep.2020.108362.

DECLARATION OF INTERESTS
The authors declare no competing interests.

Author Manuscript Author Manuscript Author Manuscript Author Manuscript

exposure to motivationally salient stimuli. Using *in vivo* two-photon calcium imaging, we find that *Pnoc*$^{\text{BNST}}$ neuronal responses directly correspond with rapid increases in pupillary size when mice are exposed to aversive and rewarding odors. Furthermore, optogenetic activation of these neurons increases pupillary size and anxiety-like behaviors but does not induce approach, avoidance, or locomotion. These findings suggest that excitatory responses in *Pnoc*$^{\text{BNST}}$ neurons encode rapid arousal responses that modulate anxiety states. Further histological, electrophysiological, and single-cell RNA sequencing data reveal that *Pnoc*$^{\text{BNST}}$ neurons are composed of genetically and anatomically identifiable subpopulations that may differentially tune rapid arousal responses to motivational stimuli.

Graphical Abstract

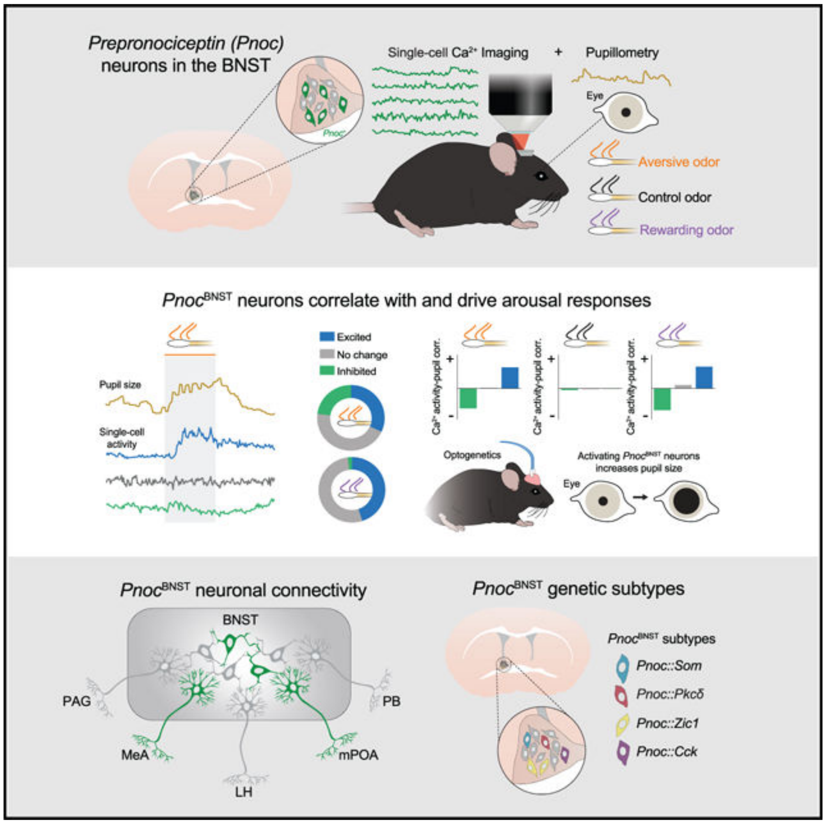

In Brief

Rodriguez-Romaguera et al. find an ensemble of neurons within the extended amygdala (BNST) that expresses the *prepronociceptin* gene and functions to encode the rapid arousal responses that are triggered by motivational stimuli.

INTRODUCTION

Dysfunctional arousal responses are a core component of many neuropsychiatric disorders. For example, patients with anxiety disorders often show hyperarousal responses to negatively salient stimuli, and patients suffering from depression show hypoarousal

Author Manuscript
Author Manuscript
Author Manuscript
Author Manuscript

responses to positively salient stimuli (Craske et al., 2009; Lang and McTeague, 2009; Patriquin et al., 2019; Schmidt et al., 2017; Urbano et al., 2017; Wilhelm and Roth, 2001). Elucidating the neural circuit elements that orchestrate changes in physiological arousal is, thus, essential for understanding maladaptive motivational states (Marton and Sohal, 2016; Sparta et al., 2013; Touriño et al., 2013). Rodent models have enabled intricate dissection of the neural circuits for both negative and positive motivational states by presenting stimuli that elicit aversion or reward (Calhoon and Tye, 2015; Stuber and Wise, 2016; Tovote et al., 2015). However, these studies often overlook the rapid increases in physiological arousal that characterize changing motivational states. In humans, rapid (within seconds) increases in physiological arousal, as measured by pupil size changes, follow exposure to negatively salient stimuli, such as threat-inducing images (Cascardi et al., 2015; Price et al., 2013). The same is true when humans are presented with positively salient stimuli, such as rewarding images of money or videos of caregivers (Schneider et al., 2018; Tummeltshammer et al., 2019). Thus, in addition to long-term adaptations in arousal (e.g., sleep/wake states; de Lecea et al., 2012), an important component of motivation is the rapid changes in physiological arousal upon presentation of salient stimuli.

One particular brain region that may encode rapid changes in arousal is the bed nucleus of the stria terminalis (BNST, a part of the extended amygdala). Evidence from anatomical (Dabrowska et al., 2011; Dong et al., 2001; Singewald et al., 2003), behavioral (Duvarci et al., 2009; Jennings et al., 2013a; Kim et al., 2013; Walker et al., 2009), and neuroimaging (Straube et al., 2007; Yassa et al., 2012) studies has implicated BNST as a key component of the neural circuitry that regulates motivated behavior. For instance, recent neurocircuit studies in mice have highlighted the role of BNST in reward and aversion (Giardino et al., 2018; Jennings et al., 2013a, 2013b; Kim et al., 2013), fear and anxiety-like behaviors (Crowley et al., 2016; Duvarci et al., 2009; Kim et al., 2013; Marcinkiewcz et al., 2016; Walker et al., 2009), and social preference and aversion (Goodson and Wang, 2006; Lei et al., 2010; Newman, 1999). Further, previous studies have identified how subsets of BNST neurons expressing certain marker genes such as corticotrophin-releasing hormone (*Crh*$^{\text{BNST}}$), protein kinase C δ (*Pkcδ*$^{\text{BNST}}$), and somatostatin (*Som*$^{\text{BNST}}$) drive motivated behaviors (Kash et al., 2015; Koob and Heinrichs, 1999; Lebow and Chen, 2016; Tovote et al., 2015). However, whether specific neural populations within BNST drive rapid changes in physiological arousal remains unknown. This is, in part, due to the low number of studies linking the functional heterogeneity within BNST with its role in rapid changes in physiological arousal (Kim et al., 2013).

Neuropeptide gene expression patterns have identified functionally distinct subpopulations of neurons in BNST (Kash et al., 2015). Recently, neurons that express the *prepronociceptin* gene (*Pnoc*, the genetic precursor to the neuropeptide nociceptin) within the central nucleus of the amygdala, the paranigral ventral tegmental area, and the arcuate nucleus of the hypothalamus were shown to have a role in gating motivational states and reward seeking (Hardaway et al., 2019; Jais et al., 2020; Parker et al., 2019). Interestingly, *Pnoc* expression within BNST is among the highest within the central nervous system (Boom et al., 1999; Ikeda et al., 1998), so we set out to investigate the role of these neurons in defining motivational states, specifically in driving the physiological arousal responses that occurs in response to motivationally salient stimuli.

Author Manuscript

Author Manuscript

Author Manuscript

Author Manuscript

In the present study, we used cell-type-specific optogenetic and head-fixed two-photon calcium-imaging approaches (McHenry et al., 2017; Namboodiri et al., 2019; Otis et al., 2017) to assess the role of *Pnoc*$^{\text{BNST}}$ neurons in driving and encoding rapid physiological arousal responses to aversive and rewarding odors. We found a variety of responses among *Pnoc*$^{\text{BNST}}$ neurons; particularly, the magnitude of correlation between neural dynamics of these neurons and pupillary responses increased with exposure to aversive and rewarding odors. We also found that excitatory responses that correlated with pupillary responses were common across both odor presentations, suggesting that motivational salience might be responsible for this response pattern. Optogenetic activation of *Pnoc*$^{\text{BNST}}$ neurons increased physiological measurements associated with arousal (pupillary response and heart rate) and further modulated anxiety-like behavior but did not induce approach, avoidance, or locomotion. Single-cell RNA sequencing revealed that *Pnoc*$^{\text{BNST}}$ neurons are transcriptionally diverse and can be subdivided by multiple distinct gene markers. Collectively, these results suggest that *Pnoc*$^{\text{BNST}}$ neurons play an important role in orchestrating arousal-related responses associated with motivationally salient stimuli.

RESULTS

Expression of *Pnoc* Defines a Subpopulation of GABAergic Neurons within adBNST that Can Be Monitored Using Calcium-Imaging Approaches

BNST is composed of various subnuclei that have unique molecular and functional identities (Giardino et al., 2018; Gungor and Paré, 2016). Therefore, we first assessed the distribution of *Pnoc*-expressing neurons across the BNST. Using fluorescent *in situ* hybridization (FISH), we observed high expression of *Pnoc* distributed throughout the BNST (Figure 1A) but particularly in the anterodorsal BNST (adBNST), as previously described (Neal et al., 1999). Further, we found that *Pnoc*$^{\text{BNST}}$ neurons predominantly express the vesicular GABA transporter gene, *Slc32a1* (*Vgat*), and not the vesicular glutamate transporter 2 gene, *Slc17a6* (*Vglut2*; Figure 1B), indicating that *Pnoc* expression defines a subpopulation of GABAergic neurons within BNST. *Pnoc*-IRES-*Cre* mice (Hardaway et al., 2019; Parker et al., 2019) were then used for selective targeting of *Pnoc*$^{+}$ neurons in adBNST in conjunction with Cre-inducible viruses.

To characterize how *Pnoc*$^{\text{BNST}}$ firing is related to calcium-mediated fluorescent dynamics, we transduced the adBNST of *Pnoc*-IRES-Cre mice with Cre-dependent GCaMP6s virus (Figure 1C). We then performed calcium imaging in brain slices under an epifluorescent microscope and simultaneously activated *Pnoc*$^{\text{BNST}}$ neurons via current injections at various frequencies. We found a linear relationship between evoked action potentials and their respective fluorescent peaks (Figures 1E–1G), demonstrating that calcium dynamics track evoked firing in brain slices.

Pnoc$^{\text{BNST}}$ Neurons Encode Rapid Changes in Arousal to Aversive and Rewarding Stimuli

Since the BNST is thought to coordinate motivational states essential for guiding actions of reward seeking and aversion (Calhoon and Tye, 2015; Kash et al., 2015; Lebow and Chen, 2016; Stamatakis et al., 2014; Tovote et al., 2015), we tested whether the activity of *Pnoc*$^{\text{BNST}}$ neurons is altered by exposure to stimuli with opposing motivational salience. We

Author Manuscript

Author Manuscript

Author Manuscript

Author Manuscript

exposed mice to either trimethylthiazoline (TMT, as an aversive odorant) or peanut oil (as an appetitive odorant) as odors that induce either place aversion or place preference (Root et al., 2014), respectively. First, we demonstrated that freely moving mice reliably avoided a location with TMT and preferred a location containing peanut oil (Figures 2A–2C), consistent with the aversive and appetitive nature of these olfactory stimuli. We also observed increases in pupillary size when freely moving mice were in proximity to either TMT- or peanut-oil-containing odor swabs, as compared to a swab with water (Figures 2D–2F). Pupillary responses have been shown to reflect rapid changes in physiological arousal (Cascardi et al., 2015; Price et al., 2013).

To evaluate encoding of *Pnoc*$^{\mathrm{BNST}}$ neurons to these odors, we developed a head-fixed behavioral preparation compatible with two-photon microscopy to control proximity of an odor swab and allow us to measure pupil dilation and ambulation (Figures 2J and 2K). Odors were presented with a cotton swab that could be positioned near or far from the mouse, while pupil size was recorded through a camera aimed at one of the eyes (Reimer et al., 2014). Having animals head-fixed also allowed us to record calcium activity from individual *Pnoc*$^{\mathrm{BNST}}$ neurons in awake mice via a GRIN lens under a two-photon microscope (Figures 2G and 2H). With algorithms that use constrained nonnegative matrix factorization (CNMF) (Pnevmatikakis et al., 2016; Zhou et al., 2018), we extracted activity dynamics from individual *Pnoc*$^{\mathrm{BNST}}$ neurons (Figure 2I; Figures S1A–S1E). We found that ~50% of *Pnoc*$^{\mathrm{BNST}}$ neurons showed a significant change in response (either excitation or inhibition) to a swab with TMT or peanut oil as compared to a control (water) swab (Figures 3A–3G). Strikingly, neurons that showed significant excitation or inhibition to TMT or peanut oil swabs showed significant increases in correlation between pupillary fluctuations and their individual neural dynamics (Figures 3H–3J). We also found different proportions of neurons that were excited and inhibited between TMT and peanut oil exposure (Figure 3G), suggesting that subtypes of *Pnoc*$^{\mathrm{BNST}}$ neurons may exist to encode aversive versus rewarding arousal states. Inhibitory responses appear to be specific to aversive arousal states, while excitatory responses were observed in both aversive and rewarding arousal states (Figure 3G). We next analyzed neurons from a subset of mice that were first exposed to the peanut swab and subsequently to the TMT swab (n = 162 neurons from 2 mice). We found that half of the neurons that were excited to the peanut swab were also excited to the TMT swab. Similarly, half of the neurons that showed no change to the peanut swab were significantly excited to the TMT swab, thus further suggesting that a subgroup of *Pnoc*$^{\mathrm{BNST}}$ neurons encodes arousal independent of the valence of the stimuli, whereas other groups encode negative arousal specifically. Taken together, we found heterogeneity in response dynamics from individual *Pnoc*$^{\mathrm{BNST}}$ neurons that correlate with pupillary responses. In summary, inhibitory responses are specific to aversive odors, whereas excitatory responses are shared across both aversive and rewarding odors, which include subgroups of *Pnoc*$^{\mathrm{BNST}}$ neurons that encode arousal independent of valence.

Pnoc$^{\mathrm{BNST}}$ activity may also relate to locomotor activity. Consistent with the valence of each odorant, the TMT swab produced an initial decrease in movement velocity when the odor was near, whereas the peanut oil swab produced a moderate increase in velocity (Figures S2A and S2B). Similar to pupil diameter, velocity and neural activity of *Pnoc*$^{\mathrm{BNST}}$ neurons showed significant correlations in neurons that showed a significant change in response

Author Manuscript

Author Manuscript

Author Manuscript

Author Manuscript

(either excitation or inhibition) to mice exposed to the peanut swab (Figures S2C–S2E). The increase in correlation was very modest to TMT exposure and occurred only in neurons excited by the TMT swab as compared to the control swab. In summary, we found that a large proportion of *Pnoc*$^{\text{BNST}}$ neurons are correlated with measurements of arousal states, and the observed heterogeneity in response dynamics that can be observed across neurons (Figure S2G) suggests that these neurons are composed of functionally distinct subtypes.

Pnoc$^{\text{BNST}}$ Neurons Drive Arousal Responses and Anxiety-like Behavior

Since we observed that excitatory responses were predominant to both motivationally salient stimuli, we next tested whether optogenetic photoactivation of *Pnoc*$^{\text{BNST}}$ neurons (Figures 4A–4C) can induce locomotion and motivational states. We first evaluated whether viral tools can reliably activate *Pnoc*$^{\text{BNST}}$ neuronal activity. Whole-cell patch-clamp slice electrophysiological recordings in adBNST within ChR2-expressing *Pnoc*$^{\text{BNST}}$ neurons (Figure 4B) showed that we could reliably photoactivate *Pnoc*$^{\text{BNST}}$ neurons at 20 Hz with 100% spike fidelity (Figures 4C and 4D). In freely moving mice, we first found that photoactivation of *Pnoc*$^{\text{BNST}}$ neurons did not induce changes in locomotion, as assessed by measuring velocity in freely moving mice (Figures 4E and 4F). To test whether photoactivation of *Pnoc*$^{\text{BNST}}$ neurons induced a place preference or aversion, freely moving mice were placed in a two-chambered arena to assess time spent in a chamber paired with photoactivation of *Pnoc*$^{\text{BNST}}$ neurons (real-time place preference assay). Photoactivation of *Pnoc*$^{\text{BNST}}$ neurons did not induce either place aversion or place preference (Figures 4G and 4H), indicating that *Pnoc*$^{\text{BNST}}$ neurons may not inherently drive locomotion or approach/avoidance behaviors.

We next wanted to test whether photoactivation of *Pnoc*$^{\text{BNST}}$ neurons was sufficient to increase physiological arousal. To accomplish this, we developed a stationary head-fixed preparation that allowed for the measurement of arousal responses in combination with optogenetics by transducing Cre-dependent channelrhodopsin into the adBNST of *Pnoc*-IRES-Cre mice (Figure 4I). Photoactivation of *Pnoc*$^{\text{BNST}}$ neurons again showed that it did not alter movement, as measured by a piezoelectric sensor underneath the mice (Figure 4J), but significantly increased both pupil area (Figure 4K) and heart rate (Figure 4L). Taken together, these data suggest that the activity of *Pnoc*$^{\text{BNST}}$ neurons increases physiological arousal responses.

Next, we tested whether the photoactivation of *Pnoc*$^{\text{BNST}}$ neurons was sufficient to drive anxiety-like behaviors in an elevated plus maze (EPM), a test traditionally used to test efficacy of anxiolytic drugs. To accomplish this, we photoactivated *Pnoc*$^{\text{BNST}}$ neurons while mice explored an EPM, which consisted of two open arms and two perpendicular closed arms. We found that photoactivation of *Pnoc*$^{\text{BNST}}$ neurons in the EPM further decreased time in the open arms (Figures 4M and 4N). Similarly, photoactivation of *Pnoc*$^{\text{BNST}}$ neurons in an open field arena also decreased time in the center of the arena (Figures S3A–S3C). We next tested whether *Pnoc*$^{\text{BNST}}$ neurons were necessary to avoid the open arms of the EPM. In agreement with our photoactivation findings, photoinhibition of *Pnoc*$^{\text{BNST}}$ neurons significantly increased time in the open arms (Figures 4O and 4P). In summary, our data

Author Manuscript Author Manuscript Author Manuscript Author Manuscript

indicate that *Pnoc*$^{\text{BNST}}$ neurons are capable of driving arousal responses independent of behavior and can modulate anxiety-like states.

***Pnoc*$^{\text{BNST}}$ Neurons Exhibit Diversity in Both Anatomical Connectivity and Genetic Identity**

Since we found heterogeneity in response dynamics with animals exposed to both arousal-inducing aversive and rewarding odors, we hypothesized that this heterogeneity may be due to the diversity of connectivity and gene expression patterns within the *Pnoc*$^{\text{BNST}}$ neuronal population. To investigate connectivity, we injected a Cre-dependent virus into the adBNST of *Pnoc*-IRES-Cre mice to express both a cytosolic marker and a presynaptic marker. We found presynaptic labeling from *Pnoc*$^{\text{BNST}}$ neurons within multiple compartments of BNST (evidenced by synaptophysin-mRuby expression), suggesting that these cells form local connections among various BNST subnuclei. Notably, we observed that presynaptic *Pnoc*$^{\text{BNST}}$ terminals overlapped with both mGFP-labeled and unlabeled cells within the BNST, indicating that *Pnoc*$^{\text{BNST}}$ neurons may form monosynaptic connections with both *Pnoc*$^{+}$ and *Pnoc*$^{-}$ neurons (Figure 5A). Whole-cell patch-clamp electrophysiological recordings revealed that light-evoked inhibitory postsynaptic currents were detected in adBNST neurons following photostimulation of *Pnoc*$^{\text{BNST}}$ neurons, which was blocked by bath application of a GABA_A receptor antagonist (gabazine; Figure 5B), confirming local connectivity and the GABAergic phenotype of these cells. Furthermore, local inhibition arising from *Pnoc*$^{\text{BNST}}$ activation was detected in a greater proportion of recorded eYFP^{-} neurons (59%, putative non-*Pnoc*$^{\text{BNST}}$ neurons) but still present in eYFP^{+} neurons (31%, *Pnoc*$^{\text{BNST}}$ neurons) (Figure 5C). Taken together, these data demonstrate that *Pnoc*$^{\text{BNST}}$ neurons form local monosynaptic inhibitory connections with both putative *Pnoc*$^{-}$ and *Pnoc*$^{+}$ BNST neurons.

To identify projection targets from *Pnoc*$^{\text{BNST}}$ neurons, we labeled these neurons (including their axonal projections) and assessed the expression of their fluorescent markers in distal target regions. Distal axonal labeling was observed predominantly within the medial amygdala (MeA) and medial preoptic area (mPOA), with sparse to near-absent labeling in other adBNST output regions, including the arcuate nucleus (ARC), lateral hypothalamic area (LHA), ventromedial hypothalamus (VMH), parabrachial nucleus (PB), and periaqueductal gray (PAG) (Figures 5D and 5E) (Calhoon and Tye, 2015; Jennings et al., 2013a; Kim et al., 2013; Lebow and Chen, 2016). The MeA and mPOA are two regions critical for social motivation (Li et al., 2017; McHenry et al., 2017); therefore *Pnoc*$^{\text{BNST}}$ projections to these regions may be involved in social arousal.

To address whether *Pnoc*$^{\text{BNST}}$ neurons are composed of distinct subpopulations of genetically identifiable neurons, we used a single-cell sequencing approach using a droplet-based method (Drop-seq) (Macosko et al., 2015) that allowed us to capture mRNA from 2,492 individual cells within the BNST (medians of 1,435 genes per cell and 2,257 per cell unique transcripts; Figures 6A and S4A–S4F). We partitioned these cells into distinct clusters using cluster analysis based on gene expression patterns (Figures 6B and S4G). Out of 19 defined clusters, 11 expressed the canonical neuronal gene *Camk2b*, whereas the remaining 8 clusters expressed known markers for non-neuronal cell types that defined astrocytes, oligodendrocytes, and oligodendrocyte precursor cells. Our single-cell

Author Manuscript Author Manuscript Author Manuscript Author Manuscript

sequencing approach revealed that *Vgat* is expressed more abundantly than *Vglut2* across all BNST neuronal clusters (Figure S4J). We found that 88% of *Pnoc*$^{\mathrm{BNST}}$ neurons were distributed among 4 of the 11 neuronal clusters (Figures 6C, 6D, S4H, and S4I) that were differentiated by the expression of somatostatin (*Som*), protein kinase C δ (*Pkcδ*), cholecystokinin (*Cck*), and the zic family member 1 (*Zic1*). Furthermore, little to no overlap (<5%) was observed between *Pnoc*$^{\mathrm{BNST}}$ neurons and neuronal clusters defined by the expression of forkhead box protein P2 (*Foxp2*), preproenkephalin (*Penk*), preprodynorphin (*Pdyn*), calbindin 2 (*Calb2*), corticotropin-releasing hormone (*Crh*), neurotensin (*Nts*), and Vglut3 (*Slc17a8*). FISH experiments corroborated a subset of our sequencing data (Figures 6E and 6F). In summary, these data suggest that *Pnoc*$^{\mathrm{BNST}}$ neurons can be further subdivided into at least 4 unique cell types identified by the coexpression of *Som*, *Pkcδ*, *Cck*, and *Zic1*.

DISCUSSION

In the present study, we found that *Pnoc* expression defines a subpopulation of GABAergic neurons within the BNST that are associated with changes in physiological arousal. *Pnoc*$^{\mathrm{BNST}}$ neurons encode the rapid increase in arousal that occurs upon the presentation of salient motivational stimuli. On their own, they are unable to alter locomotion or avoidance/approach behaviors but can bi-directionally modulate anxiety-like behavior. Further, these neurons form local monosynaptic inhibitory connections with both *Pnoc*$^{-}$ and *Pnoc*$^{+}$ neurons within the adBNST and project to both the MeA and mPOA. In agreement with the observed heterogeneity in *Pnoc*$^{\mathrm{BNST}}$ response dynamics, we found that *Pnoc*$^{\mathrm{BNST}}$ neurons can be divided into at least 4 genetically unique cell types that can be identified by co-expression of *Pnoc* with either *Som*, *Pkcδ*, *Cck*, or *Zic1*. Taken together, these data show that *Pnoc*$^{\mathrm{BNST}}$ neurons have a critical role in driving rapid arousal responses that are characteristic of a variety of motivational states and highlight the need for future studies to further unravel the heterogeneity within this genetically identified neuron population.

Elevated anxiety is a maladaptive state that is associated with many neuropsychiatric conditions (Calhoon and Tye, 2015; LeDoux and Pine, 2016; Perusini and Fanselow, 2015). The manifestation of anxiety-like states includes both behavioral and physiological responses that need to occur rapidly in order to guide actions necessary for survival. Past research has developed an expansive literature on the neural circuits governing anxiety-like behavioral actions (for reviews, see Calhoon and Tye, 2015; Harris and Gordon, 2015; Shin and Liberzon, 2010; Tovote et al., 2015), yet physiological arousal has received less attention. Excessive arousal responses as measured by increases in pupil size during threat exposure is commonly observed in patients suffering from anxiety disorders (Cascardi et al., 2015; Price et al., 2013). The presentation of negative emotionally arousing images increases both pupil size and amygdala activity (as measured by BOLD signaling) (Hermans et al., 2013), but the relationship between these two variables has remained elusive. fMRI lacks both the temporal resolution needed to match the rapid changes in pupil size and the spatial resolution to identify subregions and, more important, individual neurons. In this study, we showed that changes in the activity dynamics of individual *Pnoc*$^{\mathrm{BNST}}$ neurons are correlated with changes in pupil size and that these neurons are able to modulate anxiety-like

Author Manuscript Author Manuscript Author Manuscript Author Manuscript

behaviors. Therefore, *Pnoc*$^{\text{BNST}}$ neurons may be a critical component for orchestrating excessive physiological arousal responses in pathological anxiety.

Our findings highlight a diversity of response dynamics to salient olfactory stimuli and genetically identifiable subtypes within the *Pnoc*$^{\text{BNST}}$ neuronal population. Therefore, future studies may want to address whether diverse responses are still present during spontaneous states in the absence of motivational stimuli. Furthermore, experiments aimed at understanding the role of *Pnoc*$^{\text{BNST}}$ subtypes during specific time windows following presentation of arousal-inducing stimuli such as rewarding stimuli, omission of reward, and cues that predict them may also aid in understanding the role of this ensemble in orchestrating rapid arousal responses during more complex motivational states. It is important to note that studies that directly inhibit *Pnoc*$^{\text{BNST}}$ neurons (and functional subtypes) are needed to make causal conclusions about the role of this ensemble in driving rapid arousal responses. We found that *Pnoc*$^{\text{BNST}}$ neurons consist of an interconnected microcircuit of GABAergic neurons within the BNST that may be classified by the expression of distinct genetic markers (*Som*, *Prkcd*, *Cck*, and *Zic1*). This further suggests that either functionally distinct subtypes of *Pnoc*$^{\text{BNST}}$ neurons exist or molecularly distinct subtypes of BNST neurons share a similar function. Therefore, future studies are needed to systematically assess the causal role of *Pnoc*$^{\text{BNST}}$ neuronal subtypes and their role in rapid arousal responses. For example, co-expression of *Npy* and *Som* has been previously reported throughout the entire amygdala (McDonald, 1989), suggesting that both of these markers identify a single neuronal cell type. Our data identify a similar neuronal cluster characterized by the co-expression of *Npy* and *Som*. It was previously shown that *Npy*-expressing neurons have a specific projection output to the preoptic region of the hypothalamus (Pompolo et al., 2005). Our data show that at least a subset of *Pnoc*$^{\text{BNST}}$ neurons share this projection. Taken together, perhaps these three genetic markers (*Pnoc*, *Npy*, and *Som*) may be used to target the sub-population of *Pnoc*$^{\text{BNST}}$ neurons that project from the BNST to the mPOA. Considering the role of mPOA in social avoidance/approach behavior (McHenry et al., 2017), this projection may be important for social arousal.

A recent study showed that local photoactivation of all *Som*$^{\text{BNST}}$ neurons drives anxiety-mediated avoidance in the EPM (Ahrens et al., 2018). Therefore, how *Pnoc*$^{+}$/*Som*$^{+}$ and *Pnoc*$^{+}$/*Som*$^{-}$ neurons might differ in the regulation of anxiety-like behavior and arousal responses deserves further investigation. Additionally, future studies using intersectional genetic approaches to target *Pnoc* and either *PKCd*, *Cck*, or *Zic1* neurons could help characterize the heterogeneity of activity responses we observed in distinct *Pnoc*$^{\text{BNST}}$ subsets. It is also equally important to delineate how *Pnoc*$^{\text{BNST}}$ neurons may interact with other local *Pnoc*$^{+}$ neurons and local *Pnoc*$^{-}$ neuron clusters, such as those expressing *Foxp2*, *Penk*, *Pdyn*, *Calb2*, *Crh*, *Nts*, and *Vglut3* (Gafford and Ressler, 2015; Hammack et al., 2009; Kash et al., 2015; Lebow and Chen, 2016; McElligott and Winder, 2009; Nguyen et al., 2016).

BNST neurons have also been distinguished by their projection targets in previous studies. For instance, PB-projecting neurons regulate autonomic arousal states as measured by respiration, whereas neurons projecting to the LHA regulate anxiety-like behavior in the EPM (Kim et al., 2013; Kodani et al., 2017). A recent study showed that BNST neurons that project to the LHA can be further subdivided by the expression of the neuropeptidergic

Author Manuscript Author Manuscript Author Manuscript Author Manuscript

genes *Crh* and *Cck*. These neurons show an increase in average calcium activity specific to a rewarding (female mouse urine) or aversive odorant (TMT), respectively (Giardino et al., 2018). Furthermore, chemogenetic activation of *Vgat*-expressing neurons within the BNST increases anxiety-like behavior and leads to activation of the locus coeruleus (LC) (Mazzone et al., 2018). Although these phenotypes are similar to our findings with *Pnoc*$^{\mathrm{BNST}}$ neurons, we did not observe appreciable projections from *Pnoc*$^{\mathrm{BNST}}$ neurons to either the PB, LHA, or LC, indicating that *Pnoc*$^{\mathrm{BNST}}$ neurons may be distinct from both PB-, LHA- and LC-projecting neurons. Nonetheless, whether local interactions between *Pnoc*$^{\mathrm{BNST}}$ neurons and either PB-, LHA-, or LC-projecting neurons within the BNST exist remains an open question that warrants further investigation.

Using advanced tools to probe neurons with single-cell resolution, we discovered that *Pnoc*$^{\mathrm{BNST}}$ neurons encode rapid changes in physiological arousal responses that can drive anxiety-like behaviors. However, these neurons are likely only a piece of the complex mosaic of cell types within the BNST that contribute toward arousal responding and motivational states. Further investigations into how *Pnoc*$^{\mathrm{BNST}}$ neurons and other BNST cell types differentially and synergistically control rapid arousal responses will shed light onto how the BNST and the larger network of brain regions that regulate motivational states contribute to the development and perpetuation of neuropsychiatric disorders characterized by maladaptive motivational states.

STAR★METHODS

RESOURCE AVAILABILITY

Lead Contact—Further information and requests for resources and reagents should be directed to and will be fulfilled by the Lead Contact, Garret D. Stuber (gstuber@uw.edu).

Materials Availability—This study did not generate new unique reagents.

Data and Code Availability—The code generated during this study are available at https://github.com/stuberlab. Single cell sequencing data are available at GEO: GSE132067. All other data are available upon request from the Lead Contact.

EXPERIMENTAL MODEL AND SUBJECT DETAILS

Animals—Adult (25–30 g) male prepronociceptin-IRES-*Cre* (*Pnoc*-IRES-Cre) or wild-type mice (C57 BL6/J) were independently housed and maintained on a reverse 12-hr light-dark cycle (lights off at 08:00 AM) with *ad libitum* access to food and water. Behavior was tested during the dark cycle. All procedures were conducted in accordance with the Guide for the Care and Use of Laboratory Animals, as adopted by the National Institute of Health, and with the approval of the Institutional Animal Care and Use Committee from the University of North Carolina at Chapel Hill.

METHOD DETAILS

Fluorescent *In Situ* Hybridization—For processing tissue samples for *in situ* hybridization, mice were anesthetized with isoflurane (3.5%–4.0%) vaporized in pure

Author Manuscript Author Manuscript Author Manuscript Author Manuscript

oxygen (1 L/min), rapidly decapitated and brains immediately extracted, and flash frozen on dry ice. 18 μm thick coronal sections were collected with a cryostat under RNase-free conditions, fixed in 4% PFA for 15 min at 4°C, dehydrated in serial concentrations of ethanol (50%–100%), and processed according to instructions provided in the RNAscope kit (Advanced Cell Diagnostics, Newark, CA). Sections were hybridized with the following mixed probes: *Pnoc* (Mm-*Pnoc*, cat. no. 437881), *Vgat* (Mm-*Slc32a1*, cat. no. 319191), *Vglut2* (Mm-*Slc17a6*-C2, cat. no. 319171), *CaMKIIα* (Mm-*Camk2a*-cust-C2, cat. no. 411851). Hybridization probes used can also be found in supplementary information (Table S1). Following amplification, sections were counterstained with DAPI and coverslipped for subsequent confocal microscopy and counted using ImageJ software.

Immunohistochemistry—For processing tissue samples for immunohistochemistry, mice were euthanized with pentobarbital (50 mg.kg, 1.p.) and transcardially perfused with 0.01 M phosphate-buffered saline (PBS) and 4% paraformaldehyde (PFA). Tissue was fixed overnight in PFA at 4°C, cryoprotected with 30% sucrose in PBS, and 40 μm thick coronal sections were collected with a cryostat. Immunochemistry was performed in *Pnoc*-IRES-*Cre* mice using the following primary (kept overnight at 4°C) and secondary (kept at room temperature for 2 h) antibodies: chicken-anti-GFP (1:1,000; Aves labs, Tigard, OR), donkey anti-chicken 488 (1:500; Jackson Immuno Research Labs, West Grove, PA), mouse anti-PKCδ (1:500; BD Biosciences, Fanklin Lakes, NJ), donkey anti-mouse 647 (1:500; Jackson Immuno Research Labs, West Grove, PA), rabbit anti-Somatostatin (1:2,000; BMA Biomedicals, Switzerland), and donkey anti-rabbit 647 (1:500; Jackson Immuno Research Labs, West Grove, PA). Antibodies used with dilutions can also be found in supplementary information (Table S1). Immunoprocessing procedures were done as previously described (Jennings et al., 2013a), and sections were counterstained with DAPI and coverslipped for subsequent confocal microscopy and counted using ImageJ software.

Confocal Microscopy—A confocal microscope (Zeiss LSM 780, Carl Zeiss, San Diego, CA) with either a 20x (air), 40x (air), or a 63x (oil) objective was used to capture images. Software (Zen Software, Carl Zeiss, Jena, Germany) settings were optimized for each experiment. In general, z stacks were acquired in less than 1 μm increments and the maximum intensity projection of tiled images were used for representative images or for quantification purposes.

Viral Constructs—All viral constructs [Cre-inducible AAVdj-EF1α-DIO-GCaMP6s (3.1×10^{12} infectious units/mL), AAV5-EF1α-DIO-hChR2(H134R)-eYFP (4.3×10^{12} infectious units/mL), AAV5-EF1α-DIO-eNpHR3.0-eYFP (8.0×10^{12} infectious units/mL), AAV5-EF1α-DIO-eYFP (6.0×10^{12} infectious units/mL), and AAVdj-hSyn-Flex-mGFP-2A-synaptophysin-mRuby (5.0×10^{8} infectious units/mL)] were packaged by the UNC Vector Core and can also be found in supplementary information (Table S1).

Surgery and Histology—Mice were anesthetized with isoflurane (0.8%–1.5%) vaporized in pure oxygen (1 l/min^{-1}) and placed in a stereotaxic frame (David Kopf Instruments, Tujunga, CA). Ophthalmic ointment (Akorn, Lake Forest, IL) and topical anesthetic (2% lidocaine; Akorn, Lake Forest, IL) were applied during surgeries, and subcutaneous

Author Manuscript Author Manuscript Author Manuscript Author Manuscript

administration of saline (0.9% NaCL in water) were administered to prevent dehydration. Microinjections using injection needles (33 gauge) connected to a 2 uL syringe (Hamilton Company, Reno, NV) were used to deliver viruses into the anterior dorsal portion of the bed nucleus of the stria terminalis (adBNST; 500 nL per side; relative to bregma: +0.14 AP, +/−0.95 ML, DV −4.20 DV). For calcium imaging studies, unilateral virus injections were made into adBNST. To allow subsequent imaging of BNST neurons, a microendoscope [a gradient refractive index (GRIN) lens, 0.6 mm in diameter, 7.3 mm in length; Inscopix, Palo Alto, CA] was implanted 0.2 mm dorsal to the adBNST target site.

For optogenetic studies, bilateral virus injections were made into BNST, and an optical fiber was implanted with a 10° angle approximately 0.5 mm above the BNST. For experiments involving head-fixed behavior, a custom-made head-ring (stainless steel; 5 mm ID, 11 mm OD) was attached to the skull during surgery to allow head-fixation. Following surgeries, mice were given acetaminophen in their drinking water for 2 days and were allowed to recover with access to food and water *ad libitum* for at least 21 days. Following behavioral experiments, all cohorts were euthanized and perfused, tissue was extracted and 40 µm thick coronal sections collected with a cryostat, counterstained with DAPI and coverslipped for verification of viral expression and fiber/lens placement.

Patch-Clamp Electrophysiology—Mice were anesthetized with pentobarbital (50mg/kg) before transcardial perfusion with ice-cold sucrose cutting solution containing the following (in mM): 225 sucrose, 119 NaCl, 1.0 NaH_2PO_4, 4.9 $MgCl_2$, 0.1 $CaCl_2$, 26.2 $NaHCO_3$, 1.25 glucose, 305 mOsm. Brains were then rapidly removed, and 300 µm thick coronal sections containing BNST were taken using a vibratome (Leica, VT 1200, Germany). Sections were then incubated in aCSF (32°C) containing the following (in mM): 119 NaCl, 2.5 KCl, 1.0 NaH_2P0_4, 1.3 MgCl, 2.5 $CaCl_2$, 26.2 $NaHCO_3$, 15 glucose, ~306 mOsm. After an hour of recovery, slices were constantly perfused with aCSF (32°C) and visualized using differential interference contrast through a 40x water-immersion objective mounted on an upright microscope (Olympus BX51WI, Center Valley, PA). Recordings were obtained using borosilicate pipettes (3–5 MΩ) back-filled with internal solution containing the following (in mM): 130 K gluconate, 10 KCl, 10 HEPES, 10 EGTA, 2 $MgCl_2$, 2 ATP, 0.2 GTP (pH 7.35, 270–285 mOsm.

Current-clamp recordings were obtained from GCaMP6s-expressing *Pnoc*^{BNST} neurons to identify how action potential frequency correlated with GCaMP6s fluorescence as previously described (Otis et al., 2017). Specifically, to determine how elevations in action potential frequency influence GCaMP6s fluorescence, a 1 s train of depolarizing pulses (2 nA, 2 ms) was applied at a frequency of 1, 2, 5, 10, or 20 Hz. During electrophysiological recordings, GCaMP6s fluorescence dynamics were visualized using a mercury lamp (Olympus U-RFL-T, Center Valley, PA) and a microscope-mounted camera (QImaging, optiMOS, Canada). Imaging data were acquired using Micro-Manager and extracted through hand-drawn ROIs for each recorded neuron using ImageJ. In addition to these experiments, we also performed current-clamp recordings to determine the spike fidelity of *Pnoc*^{BNST} ChR2-expressing neurons during optogenetic stimulation. To do so, neurons were held at resting membrane potential (n = 7), and a blue LED (490nm; 1 mW) was presented in a

Author Manuscript Author Manuscript Author Manuscript Author Manuscript

series of 10 pulses (5 ms per pulse) at 1, 5, 10, and 20 Hz. We found that every pulse evoked an action potential for all neurons, suggesting 100% spike fidelity across cells.

Voltage-clamp recordings were obtained from BNST ChR2-expressing neurons (*Pnoc*$^+$), and BNST non-ChR2 expressing neurons (*Pnoc*$^-$) to identify local synaptic innervation of *Pnoc*$^{\text{BNST}}$ neurons. To determine if a neuron was *Pnoc*$^+$, we held all cells at −70mV and tested for the presence of ChR2 by displaying a blue LED (490nm; < 1mW) for 1 s. In the case that a long, stable inward current was evoked for the duration of that sweep, the neuron was confirmed to be *Pnoc*$^+$ and ChR2$^+$ (n = 26). Otherwise, the neuron was assumed to be *Pnoc*$^-$ and ChR2$^-$ (n = 37). We did not detect the presence of any transient, optically-evoked excitatory postsynaptic current (oeEPSC) during these sweeps, suggesting that *Pnoc*$^{\text{BNST}}$ neurons do not release excitatory transmitters within this circuit. Next, we held all neurons at the reversal potential for ChR2 (+5 to +15 mV for *Pnoc*$^+$ neurons; +10 mV for *Pnoc*$^-$ neurons) and tested for the presence of an optically-evoked inhibitory postsynaptic current (oeIPSC) by displaying the blue LED for 5 ms. In a subset of cells, we tested whether the oeIPSC was mediated by GABA$_A$ receptors by bath-applying GABAzine (10 uM) for 5 minutes. For all voltage-clamp experiments, data acquisition occurred at a 10 kHz sampling rate. All patch-clamp recordings were made through a MultiClamp 700B amplifier connected to a Digidata 1440A digitizer (Molecular Devices, San Jose, CA) and analyzed using Clampfit 10.3 (Molecular Devices, San Jose, CA).

Odor Preference in Freely-moving Mice—Mice were habituated to have a square block holder in their home cage for 2 days prior to testing. The day of testing, a cotton swab was placed in the square block holder located in an upright position 4 in from the home cage floor on one of the sides (sides were alternated across all mice). Mice behavior was recorded for a 5-min period after placing 2.5 μL of water (distilled H_2O) in the cotton swab, followed by placing either 2.5 μL of TMT or 2.5 μL of Peanut oil (same as head-fixed experiment) in the cotton swab. Distance to odor (cm, max: 25 cm), time spent freezing (s), and velocity (cm/s) were calculated using automated tracking software (Ethovision XT 11, Noldus, Leesburg, VA). Similar to head-fixed odor exposure experiments, a low dose of TMT was used to minimize freezing responses and maintain ambulation.

Pupil recordings were made in freely moving animals using the same camera system used for head-fixed experiments but using a triangle shape arena of similar size to the home cage with one of the corners having a 45-degree angle where the cotton swab was placed. A transparent plexiglass wall would allow viewing of the pupil when mice explored the cotton swab at close proximity. Images of the pupil where captured during the first 10 s bouts of exploration.

Two-Photon Calcium Imaging in Head-fixed Mice—A two-photon microscope (FVMPE-RS, Olympus, Center Valley, PA) was used to visualize activity dynamics of *Pnoc*$^+$ neurons in BNST *in vivo* in head-fixed mice while they underwent odor exposure with pupillometry. A virus encoding the Cre-dependent calcium indicator GCaMP6s (AAVdj-EF1α-DIO-GCaMP6s; 3.1×10^{12} infectious units/mL) was injected into BNST of *Pnoc*-IRES-Cre mice (see Surgery and histology section). After a minimum of 8 weeks to allow sufficient time for virus transport and infection, mice underwent the head-fixed freely

Author Manuscript

Author Manuscript

Author Manuscript

Author Manuscript

moving odor exposure assay described above, during which GCaMP6s-expressing neurons were visualized using two-photon microscopy.

The two-photon microscope used was equipped with the following to allow imaging of BNST *in vivo*: a hybrid scanning core set with galvanometers and fast scan resonant scanners (which allows up to 30 Hz frame -rate acquisition; set at 5 Hz), GaAsP-PMT photo detectors with adjustable voltage, gain, and offset features, a single green/red NDD filter cube, a long working distance 20x objective (air) designed for optical transmission at infrared wavelengths (LCPLN20XIR, 0.45 NA, 8.3 mm WD, Olympus, Center Valley, PA), a software-controlled modular *xy* stage loaded on a manual *z*-deck, and a tunable Mai-Tai Deep See laser system (laser set to 955 nm, ~100 fs pulse width, Spectra Physics, Santa Clara, CA) with automated four-axis alignment. Prior to testing, the optimal field of view (FOV) was selected by adjusting the imaging plane (*z*-axis). Two-photon scanning was triggered by an Arduino microcontroller and video was collected for each testing epoch (baseline, water or odor). Data were both acquired and processed using FluoView FV1200 and CellSens software packages (Olympus, Center Valley, PA). Following data acquisition, videos were motion corrected using a planar hidden Markov model (SIMA v1.3) (Kaifosh et al., 2014), calcium transients and deconvolved events were extracted from individual ROI's using constraint non-negative matrix factorization algorithms (CNMF) (Zhou et al., 2018) and data was analyzed using custom data analysis pipelines written in Python (see Quantification and Statistical Analysis section).

Head-fixed Odor Swab Exposure with Pupillometry—For exposing odors in head-fixed freely moving mice, experimental events and behavioral recordings were orchestrated using custom-designed hardware interfaced with microcontrollers (Arduino) and Python using custom code. Odor delivery relied on a custom-made conveyor system that carried a cotton swab with odor source along a 25-cm track over 6 s to and from the animal. The cotton swab remained in close proximity to the animal for a 10 s bout. We assessed locomotor activity of head-fixed animals using a custom-made running disc. The disc was fixed under the head-fixed animal, which allowed movement similar to a rodent flying saucer wheel. Rotational changes were measured by a rotary encoder (Sparkfun, Boulder, CO) every 50 ms without regard to direction of rotation. Pupil recordings were made using a monochromatic CMOS camera with macro zoom lens (MVL7000 & DCC1545M, ThorLabs, Newton, NJ) at 10 frames per second. An infrared light (Thorlabs, Newton, NJ) was used to illuminate the eye in optogenetic experiments. For two-photon experiments, the illumination light from the objective was sufficient to visualize the eye (here the light transmitted through nervous tissue and out the pupil, thus the pupil was brighter than the cornea). An ultraviolet light (Thorlabs, Newton, NJ) was used to adjust the pupil size to avoid a ceiling or floor effect of pupil changes as necessary.

Experimentation began after minimal pupillary responses were observed to the approaching of a dry cotton swab (6 days). The day of testing, mice were exposed to 3 epochs (5 minutes each) that consisted of 5 baseline bouts (dry cotton swab), 5 control bouts (cotton swab with 2.5 μL of distilled H_2O), and 5 odor bouts (cotton swab with wither 2.5 μL of TMT or 2.5 μL of Peanut oil). The first 2 bouts of each epoch were used for analysis to assess responses. A low dose of TMT was used to minimize freezing responses and maintain ambulation.

Author Manuscript Author Manuscript Author Manuscript Author Manuscript

Pupil changes were assessed offline after experimentation. A median filter was applied to each pupil recording frame before pupil diameter was measured. We used OpenCV to identify the pupil within each frame and morphological processing (erosion and dilation) to further filter noise from the image. The diameter of the pupil was measured by fitting a bounding box, and the length of its horizontal sides were used as the pupil diameter since this also measured pupil diameter fairly well during mid-blink. Calculated diameter measures were then filtered using a rolling 1 s median filter.

Optogenetics—Optogenetic experiments were performed as previously described (Sparta et al., 2011). Briefly, a virus encoding the Cre-inducible channel-rhodopsin-2 (AAV5-ef1α-DIO-hChR2(H134R)-eYFP; 5.0×10^{12} infectious units per ml) was injected into BNST of either *Pnoc*-IRES-Cre mice or their wild-type littermates as controls. For photoactivation manipulations in ChR2 or control mice, the laser (473 nm; 8–10 mW) was turned on for 5-ms pulses (20 Hz) during a 3 min period, followed or preceded by 3 min periods were the laser was off. All mice were habituated to the tether for 3 days prior to behavioral testing. Following behavioral experiments, histological verification of fluorescence and optical fiber placement were performed.

Real-Time Place Preference—Mice were placed into a rectangular two-compartment arena (52.5 × 25.5 × 25.5 cm) as previously described (Jennings et al., 2013a). Mice were allowed to freely explore the arena for 20 min. Entry into one of the compartments triggered constant 20 Hz photostimulation (473 nm; 8–10 mW). Entry into the other chamber ended the photostimulation. The side paired with photostimulation was counterbalanced across mice. Time spent in the stimulation side was calculated using automated tracking software (Ethovision XT 11, Noldus, Leesburg, VA).

Head-fixed Stationary Assay with Pupillometry—Mice were head-fixed as previously described (Otis et al., 2017). Physiological and licking measures were obtained using a custom designed apparatus. A piezo sensor under the mouse monitored general movement in the tube. A pulse oximeter placed near the neck was used to measure heart rate. Mice received unpredictable drops of sucrose (10% in water, 2.0–2.5 μl, ~ drop/min) for 30 min using a gravity-driven solenoid through a ~18-G steel tube. Mice were habituated to the setup for 6 days. Measurements were recorded using a LabJack data acquisition box (U12 Series, LabJack Corp., Lakewood, CO). Once mice habituated to the apparatus, as evident by a reduced heart rate as compared to Day 1 (6 days), optogenetic experiments were performed while pupil videos, movement (piezo sensor) and heart rate (pulse oximeter) was tracked with an Arduino microcontroller and recorded with custom software (written in Python) during a single laser off (3 min) and laser on (3 min) period.

Elevated Plus Maze—Mice were placed in a standard elevated plus maze (EPM; 13. 5 in height; 25 in × 2 in for each arm, 7 in tall wall for closed arms, 0.5 in tall/wide ledge for open arms). Mice were placed in the center of the EPM and allowed to freely explore it for 10 min. Distance to center (cm) and time spent in each arm (s) were calculated using automated tracking software (Ethovision XT 11, Noldus, Leesburg, VA).

Author Manuscript

Author Manuscript

Author Manuscript

Author Manuscript

Tissue Isolation and Single-cell cDNA Library Preparation—Mice were anesthetized with 390 g/kg sodium pentobarbital, 500 mg/kg phenytoin sodium and transcardially perfused with 20 mL in ice-cold sodium-substituted aCSF (NMDG-aCSF: 96 mM NMDG, 2.5 mM KCl, 1.35 mM NaH_2PO_4, 30 mM $NaHCO_3$, 20 mM HEPES, 25 mM glucose, 2 mM thiourea, 5 mM Na^+ascorbate, 3 mM Na^+pyruvate, 0.6 mM glutathione-ethyl-ester, 2 mM N-acetyl-cysteine, 0.5 mM $CaCl_2$, 10 mM $MgSO_4$; pH 7.35–7.40, 300–305 mOsm) modified from Ting et al. (2014). Brains were isolated and three 300 μm sections beginning at ~0.45 mm Bregma were collected in ice-cold NMDG-aCSF on a vibratome (Leica, VT 1200, Germany). Sections from 6 mice at a time (total of 4 batches with 24 mice) were recovered in NMDG-aCSF supplemented with 500 nM TTX, 10 μM APV, 10 μM DNQX (NMDG-aCSF-R) for 15 minutes after the addition of the last slice. The BNST was then isolated with 0.75 and 0.50 mm Palkovitz punches and digested in NMDG-aCSF-R containing 1.0 mg/mL pronase for 30 minutes at room temperature. Tissue was then triturated with a patch pipet fire-polished to an internal diameter of 300 μm in 1.0 mL of NMDG-aCSF-R supplemented with 0.05% BSA (NMDG-aCSF-BSA) to dissociate. The suspension transferred to 12 mL NMDG-aCSF-BSA and sedimented at 220 × *g* for 6 minutes at 18°C to wash. The supernatant was removed, and cells were resuspended in 1 mL NMDG-aCSF-BSA. To fix the cells (Alles et al., 2017), 4.0 mL of ice-cold 100% methanol was added dropwise to the suspension while gently swirling the tube. Cells were then incubated for 30 minutes on ice and transferred to −80°C. To rehydrate suspensions prior to Drop-seq, cells were removed from −80°C and incubated on ice for 15 minutes. Cells were then sedimented at 500 × *g* for 5 minutes at 4°C, resuspended in 5 mL of PBS supplemented with 0.01% BSA (PBS-BSA), and incubated for 5 minutes on ice. The suspension was then sedimented at 220 × *g* for 6 minutes at 18°C and resuspended in 1.0 mL of PBS-BSA for a final concentration of ~$2.6–3.2 \times 10^5$ cells/mL. Rehydration and droplet generation was performed on fixed samples within 3 weeks of fixation.

Drop-seq was performed as previously described in with modifications (Macosko et al., 2015). Single-cell capture was performed on a glass microfluidics device (Dolomite Microfluidics, United Kingdom) with aqueous flow at 40 μL/min and oil at 200 μL/min. Beads were loaded at ~200 beads/μL. Reverse transcription, ExoI digestion, and PCR were performed as previously described, but with 11 cycles for second stage of amplification. PCR products were pooled by batch, purified on SPRI beads (Axygen, Union City, CA), and indexed using Nextera XT with 800 *p*g input per batch. Purified tagmentation products were pooled by mass according to the estimated number of cells per pool member as quantified by a Qubit dsDNA HS Assay. Sequencing was performed at the UNC High Throughput Sequencing Facility on a lllumina HiSeq2500 using Paired-End 2×50 Rapid Run v2 chemistry.

QUANTIFICATION AND STATISTICAL ANALYSIS

Behavioral Optogenetics and Electrophysiology Data Analysis—For data obtained from the optogenetic and patch-clamp electrophysiology experiments, data were analyzed using Prism 7 (GraphPad Sotware Inc., La Jolla, CA). Mean values are accompanied by SEM values. Comparisons were tested using paired or unpaired t tests. Two-way ANOVA tests followed by either Tukey’s post hoc tests or Bonferroni post hoc

Author Manuscript Author Manuscript Author Manuscript Author Manuscript

comparisons were applied for comparisons with more than two groups, n.s. $p > 0.05$, $*p < 0.05$, $**p < 0.01$, $***p < 0.001$.

Calcium Imaging Analysis—Calcium imaging recordings were first motion corrected using a planar hidden Markov model (Kaifosh et al., 2014). Neurons were identified, and their calcium signals were extracted using a modified version of constrained nonnegative matrix factorization (CNMF) (Zhou et al., 2018), allowing us to segregate spatially overlapping signals. This extracted signal was adjusted (scaled) to account for variations in fluorescence intensities among cells by the standard deviation of a neuron's fluorescence throughout the Control odor exposure. For head-fixed, odor-presentation experiments, neuronal activity was aligned to the presentation of the odor. Neurons were classified as excitatory or inhibitory to proximity of TMT or Peanut oil if the fluorescence values for frames differed between near and far location—defined using a Mann-Whitney U test with Bonferroni correction. Correlations in activity and behavior were calculated using the Spearman correlation coefficient.

Single-Cell Sequencing Clustering and Analysis—Demultiplexing was performed allowing 1 mismatch with Illumina bcl2fastq v2.18.0.12. Initial processing and generation of digital expression matrices was performed with Drop-seq_tools v1.12 and Picard Tools v2.2.4 (Macosko et al., 2015). Alignment was performed using STAR v2.4.2a with 72 GB of RAM and 16 threads. Clustering was performed in R using Seurat v1.4.0.16 unless otherwise noted. Prior to clustering, cells were filtered by ≥ 500 unique genes, ≤ 20,000 unique molecules, and ≤ 5 percent mitochondrial reads. Filtered data was scaled to the median number of unique molecules and log(x+1) transformed. Zero-variance genes were removed from the data, and batch correction was performed with ComBat (Johnson et al., 2007) from SVA v3.220 (Leek et al., 2012) using parametric adjustment on a model matrix containing number of unique genes and molecules, and percent mitochondrial reads. Four batches were included, each containing six animals that were pooled during tissue isolation. Relative log expression by cell and mean expression correlation across batches were used to assess the correction. Only genes detected in all batches were included in the analysis.

Variable genes were selected with a cutoff of 0.5 standard deviations from the mean dispersion within a bin (Macosko et al., 2015). Variable genes were used as the basis for principal components analysis, and cluster calling was performed on principal components using the Louvain algorithm with multilevel refinement under default settings. Principal components were reduced and visualized via t-distributed stochastic neighbor embedding (tSNE) using the first 20 components and a resolution of 1.3. Clusters were reordered on a hierarchically-clustered distance matrix based on all genes. Features were identified using a single-cell likelihood-ratio test[6] implemented in Seurat. To identify cluster-specific features, genes in each cluster were tested against those in either the nearest cluster or node in the hierarchically-clustered dendrogram. Analysis from pre-processing to digital expression matrices were run on a Dell blade-based cluster running RedHat Enterprise Linux 5.6. Cluster calling and tSNE were run on a similar cluster running RedHat Enterprise Linux 7.3. All other steps were run on macOS 10.13.3.

Author Manuscript

Author Manuscript

Author Manuscript

Author Manuscript

Supplementary Material

Refer to Web version on PubMed Central for supplementary material.

ACKNOWLEDGMENTS

We thank Hiroyuki K. Kato, Anthony Burgos-Robles, Maria M. Diehl, Fabricio H. Do-Monte, Ivan Trujillo-Pisanty, and Gregory J. Quirk for helpful discussions and comments on the manuscript. We thank K. Deisseroth and the GENIE project at Janelia Research Campus for viral constructs. This work was supported by the National Institute of Mental Health (F32-MH113327 to J.R.-R., F30-MH115693 to R.L.U., K99-MH118422 to V.M.K.N., T32-MH093315 and K99-MH115165 to J.A.M., and R01-MH112355 to M.R.B.), National Institute of Neurological Disorders and Stroke (T32-NS007431 to R.L.U.), National Heart, Lung, and Blood Institute (R01-HL150836 to M.R.B.), National Institute on Drug Abuse (F32-DA041184 to J.M.O. and R37-DA032750 and R01-DA038168 to G.D.S.), Children's Tumor Foundation (016-01-006 to J.E.R.), Brain and Behavior Research Foundation (to V.M.K.N. and G.D.S.), Yang Biomedical Scholars Award (to G.D.S.), Foundation of Hope (to G.D.S.), UNC Neuroscience Center (to G.D.S.), Helen Lyng White Fellowship (to V.M.K.N.), UNC Neuroscience Center Microscopy Core (P30-NS045892), and UNC Department of Psychiatry (to G.D.S.).

REFERENCES

Ahrens S, Wu MV, Furlan A, Hwang G-R, Paik R, Li H, Penzo MA, Tollkuhn J, and Li B (2018). A Central Extended Amygdala Circuit That Modulates Anxiety. J. Neurosci 38, 5567–5583. [PubMed: 29844022]

Alles J, Karaiskos N, Praktiknjo SD, Grosswendt S, Wahle P, Ruffault P-L, Ayoub S, Schreyer L, Boltengagen A, Birchmeier C, et al. (2017). Cell fixation and preservation for droplet-based single-cell transcriptomics. BMC Biol 15, 44. [PubMed: 28526029]

Boom A, Mollereau C, Meunier JC, Vassart G, Parmentier M, Vanderhaeghen JJ, and Schiffmann SN (1999). Distribution of the nociceptin and nocistatin precursor transcript in the mouse central nervous system. Neuroscience 91, 991–1007. [PubMed: 10391477]

Calhoon GG, and Tye KM (2015). Resolving the neural circuits of anxiety. Nat. Neurosci 18, 1394–1404. [PubMed: 26404714]

Cascardi M, Armstrong D, Chung L, and Paré D (2015). Pupil Response to Threat in Trauma-Exposed Individuals With or Without PTSD. J. Trauma. Stress 28, 370–374. [PubMed: 26215078]

Craske MG, Rauch SL, Ursano R, Prenoveau J, Pine DS, and Zinbarg RE (2009). What is an anxiety disorder? Depress. Anxiety 26, 1066–1085. [PubMed: 19957279]

Crowley NA, Bloodgood DW, Hardaway JA, Kendra AM, McCall JG, Al-Hasani R, McCall NM, Yu W, Schools ZL, Krashes MJ, et al. (2016). Dynorphin Controls the Gain of an Amygdalar Anxiety Circuit. Cell Rep. 14, 2774–2783. [PubMed: 26997280]

Dabrowska J, Hazra R, Ahern TH, Guo J-D, McDonald AJ, Mascagni F, Muller JF, Young LJ, and Rainnie DG (2011). Neuroanatomical evidence for reciprocal regulation of the corticotrophin-releasing factor and oxytocin systems in the hypothalamus and the bed nucleus of the stria terminalis of the rat: Implications for balancing stress and affect. Psychoneuroendocrinology 36, 1312–1326. [PubMed: 21481539]

de Lecea L, Carter ME, and Adamantidis A (2012). Shining light on wakefulness and arousal. Biol. Psychiatry 71, 1046–1052. [PubMed: 22440618]

Dong HW, Petrovich GD, and Swanson LW (2001). Topography of projections from amygdala to bed nuclei of the stria terminalis. Brain Res. Brain Res. Rev 38, 192–246. [PubMed: 11750933]

Duvarci S, Bauer EP, and Paré D (2009). The bed nucleus of the stria terminalis mediates inter-individual variations in anxiety and fear. J. Neurosci 29, 10357–10361. [PubMed: 19692610]

Gafford GM, and Ressler KJ (2015). GABA and NMDA receptors in CRF neurons have opposing effects in fear acquisition and anxiety in central amygdala vs. bed nucleus of the stria terminalis. Horm. Behav 76, 136–142. [PubMed: 25888455]

Giardino WJ, Eban-Rothschild A, Christoffel DJ, Li S-B, Malenka RC, and de Lecea L (2018). Parallel circuits from the bed nuclei of stria terminalis to the lateral hypothalamus drive opposing emotional states. Nat. Neurosci 21, 1084–1095. [PubMed: 30038273]

Author Manuscript Author Manuscript Author Manuscript Author Manuscript

Goodson JL, and Wang Y (2006). Valence-sensitive neurons exhibit divergent functional profiles in gregarious and asocial species. Proc. Natl. Acad. Sci. USA 103, 17013–17017. [PubMed: 17071744]

Gungor NZ, and Paré D (2016). Functional Heterogeneity in the Bed Nucleus of the Stria Terminalis. J. Neurosci 36, 8038–8049. [PubMed: 27488624]

Hammack SE, Guo J-D, Hazra R, Dabrowska J, Myers KM, and Rainnie DG (2009). The response of neurons in the bed nucleus of the stria terminalis to serotonin: implications for anxiety. Prog. Neuropsychopharmacol. Biol. Psychiatry 33, 1309–1320. [PubMed: 19467288]

Hardaway JA, Halladay LR, Mazzone CM, Pati D, Bloodgood DW, Kim M, Jensen J, DiBerto JF, Boyt KM, Shiddapur A, et al. (2019). Central Amygdala Prepronociceptin-Expressing Neurons Mediate Palatable Food Consumption and Reward. Neuron 102, 1037–1052.e7. [PubMed: 31029403]

Harris AZ, and Gordon JA (2015). Long-range neural synchrony in behavior. Annu. Rev. Neurosci 38, 171–194. [PubMed: 25897876]

Hermans EJ, Henckens MJAG, Roelofs K, and Fernández G (2013). Fear bradycardia and activation of the human periaqueductal grey. Neuroimage 66, 278–287. [PubMed: 23110885]

Ikeda K, Watanabe M, Ichikawa T, Kobayashi T, Yano R, and Kumanishi T (1998). Distribution of prepro-nociceptin/orphanin FQ mRNA and its receptor mRNA in developing and adult mouse central nervous systems. J. Comp. Neurol 399, 139–151. [PubMed: 9725707]

Jais A, Paeger L, Sotelo-Hitschfeld T, Bremser S, Prinzensteiner M, Klemm P, Mykytiuk V, Widdershooven PJM, Vesting AJ, Grzelka K, et al. (2020). PNOC$^{\mathrm{ARC}}$ Neurons Promote Hyperphagia and Obesity upon High-Fat-Diet Feeding. Neuron 106, 1009–1025.e10. [PubMed: 32302532]

Jennings JH, Sparta DR, Stamatakis AM, Ung RL, Pleil KE, Kash TL, and Stuber GD (2013a). Distinct extended amygdala circuits for divergent motivational states. Nature 496, 224–228. [PubMed: 23515155]

Jennings JH, Rizzi G, Stamatakis AM, Ung RL, and Stuber GD (2013b). The inhibitory circuit architecture of the lateral hypothalamus orchestrates feeding. Science 341, 1517–1521. [PubMed: 24072922]

Johnson WE, Li C, and Rabinovic A (2007). Adjusting batch effects in microarray expression data using empirical Bayes methods. Biostatistics 8, 118–127. [PubMed: 16632515]

Kaifosh P, Zaremba JD, Danielson NB, and Losonczy A (2014). SIMA: Python software for analysis of dynamic fluorescence imaging data. Front. Neuroinform 8, 80. [PubMed: 25295002]

Kash TL, Pleil KE, Marcinkiewcz CA, Lowery-Gionta EG, Crowley N, Mazzone C, Sugam J, Hardaway JA, and McElligott ZA (2015). Neuropeptide regulation of signaling and behavior in the BNST. Mol. Cells 38, 1–13. [PubMed: 25475545]

Kim S-Y, Adhikari A, Lee SY, Marshel JH, Kim CK, Mallory CS, Lo M, Pak S, Mattis J, Lim BK, et al. (2013). Diverging neural pathways assemble a behavioural state from separable features in anxiety. Nature 496, 219–223. [PubMed: 23515158]

Kodani S, Soya S, and Sakurai T (2017). Excitation of GABAergic Neurons in the Bed Nucleus of the Stria Terminalis Triggers Immediate Transition from Non-Rapid Eye Movement Sleep to Wakefulness in Mice. J. Neurosci 37, 7164–7176. [PubMed: 28642284]

Koob GF, and Heinrichs SC (1999). A role for corticotropin releasing factor and urocortin in behavioral responses to stressors. Brain Res 848, 141–152. [PubMed: 10612706]

Lang PJ, and McTeague LM (2009). The anxiety disorder spectrum: fear imagery, physiological reactivity, and differential diagnosis. Anxiety Stress Coping 22, 5–25. [PubMed: 19096959]

Lebow MA, and Chen A (2016). Overshadowed by the amygdala: the bed nucleus of the stria terminalis emerges as key to psychiatric disorders. Mol. Psychiatry 21, 450–463. [PubMed: 26878891]

LeDoux JE, and Pine DS (2016). Using Neuroscience to Help Understand Fear and Anxiety: A Two-System Framework. Am. J. Psychiatry 173, 1083–1093. [PubMed: 27609244]

Leek JT, Johnson WE, Parker HS, Jaffe AE, and Storey JD (2012). The sva package for removing batch effects and other unwanted variation in high-throughput experiments. Bioinformatics 28, 882–883. [PubMed: 22257669]

Author Manuscript Author Manuscript Author Manuscript Author Manuscript

Lei K, Cushing BS, Musatov S, Ogawa S, and Kramer KM (2010). Estrogen receptor-alpha in the bed nucleus of the stria terminalis regulates social affiliation in male prairie voles (Microtus ochrogaster). PLoS ONE 5, e8931. [PubMed: 20111713]

Li Y, Mathis A, Grewe BF, Osterhout JA, Ahanonu B, Schnitzer MJ, Murthy VN, and Dulac C (2017). Neuronal Representation of Social Information in the Medial Amygdala of Awake Behaving Mice. Cell 171, 1176–1190.e17. [PubMed: 29107332]

Macosko EZ, Basu A, Satija R, Nemesh J, Shekhar K, Goldman M, Tirosh I, Bialas AR, Kamitaki N, Martersteck EM, et al. (2015). Highly Parallel Genome-wide Expression Profiling of Individual Cells Using Nanoliter Droplets. Cell 161, 1202–1214. [PubMed: 26000488]

Marcinkiewcz CA, Mazzone CM, D'Agostino G, Halladay LR, Hardaway JA, DiBerto JF, Navarro M, Burnham N, Cristiano C, Dorrier CE, et al. (2016). Serotonin engages an anxiety and fear-promoting circuit in the extended amygdala. Nature 537, 97–101. [PubMed: 27556938]

Marton TF, and Sohal VS (2016). Of Mice, Men, and Microbial Opsins: How Optogenetics Can Help Hone Mouse Models of Mental Illness. Biol. Psychiatry 79, 47–52. [PubMed: 25981174]

Mazzone CM, Pati D, Michaelides M, DiBerto J, Fox JH, Tipton G, Anderson C, Duffy K, McKlveen JM, Hardaway JA, et al. (2018). Acute engagement of G_q-mediated signaling in the bed nucleus of the stria terminalis induces anxiety-like behavior. Mol. Psychiatry 23, 143–153. [PubMed: 27956747]

McDonald AJ (1989). Coexistence of somatostatin with neuropeptide Y, but not with cholecystokinin or vasoactive intestinal peptide, in neurons of the rat amygdala. Brain Res. 500, 37–45. [PubMed: 2575006]

McElligott ZA, and Winder DG (2009). Modulation of glutamatergic synaptic transmission in the bed nucleus of the stria terminalis. Prog. Neuropsychopharmacol. Biol. Psychiatry 33, 1329–1335. [PubMed: 19524008]

McHenry JA, Otis JM, Rossi MA, Robinson JE, Kosyk O, Miller NW, McElligott ZA, Budygin EA, Rubinow DR, and Stuber GD (2017). Hormonal gain control of a medial preoptic area social reward circuit. Nat. Neurosci 20, 449–458. [PubMed: 28135243]

Namboodiri VMK, Otis JM, van Heeswijk K, Voets ES, Alghorazi RA, Rodriguez-Romaguera J, Mihalas S, and Stuber GD (2019). Single-cell activity tracking reveals that orbitofrontal neurons acquire and maintain a long-term memory to guide behavioral adaptation. Nat. Neurosci 22, 1110–1121. [PubMed: 31160741]

Neal CR Jr., Mansour A, Reinscheid R, Nothacker HP, Civelli O, and Watson SJ Jr. (1999). Localization of orphanin FQ (nociceptin) peptide and messenger RNA in the central nervous system of the rat. J. Comp. Neurol 406, 503–547. [PubMed: 10205026]

Newman SW (1999). The medial extended amygdala in male reproductive behavior. A node in the mammalian social behavior network. Ann. N Y Acad. Sci 877, 242–257. [PubMed: 10415653]

Nguyen AQ, Dela Cruz JA, Sun Y, Holmes TC, and Xu X (2016). Genetic cell targeting uncovers specific neuronal types and distinct subregions in the bed nucleus of the stria terminalis. J. Comp. Neurol 524, 2379–2399. [PubMed: 26718312]

Otis JM, Namboodiri VMK, Matan AM, Voets ES, Mohorn EP, Kosyk O, McHenry JA, Robinson JE, Resendez SL, Rossi MA, and Stuber GD (2017). Prefrontal cortex output circuits guide reward seeking through divergent cue encoding. Nature 543, 103–107. [PubMed: 28225752]

Parker KE, Pedersen CE, Gomez AM, Spangler SM, Walicki MC, Feng SY, Stewart SL, Otis JM, Al-Hasani R, McCall JG, et al. (2019). A Paranigral VTA Nociceptin Circuit that Constrains Motivation for Reward. Cell 178, 653–671.e19. [PubMed: 31348890]

Patriquin MA, Hartwig EM, Friedman BH, Porges SW, and Scarpa A (2019). Autonomic response in autism spectrum disorder: Relationship to social and cognitive functioning. Biol. Psychol 145, 185–197. [PubMed: 31078720]

Perusini JN, and Fanselow MS (2015). Neurobehavioral perspectives on the distinction between fear and anxiety. Learn. Mem 22, 417–425. [PubMed: 26286652]

Pnevmatikakis EA, Soudry D, Gao Y, Machado TA, Merel J, Pfau D, Reardon T, Mu Y, Lacefield C, Yang W, et al. (2016). Simultaneous Denoising, Deconvolution, and Demixing of Calcium Imaging Data. Neuron 89, 285–299. [PubMed: 26774160]

Author Manuscript Author Manuscript Author Manuscript Author Manuscript

Pompolo S, Ischenko O, Pereira A, Iqbal J, and Clarke IJ (2005). Evidence that projections from the bed nucleus of the stria terminalis and from the lateral and medial regions of the preoptic area provide input to gonadotropin releasing hormone (GNRH) neurons in the female sheep brain. Neuroscience 132, 421–436. [PubMed: 15802194]

Price RB, Siegle GJ, Silk JS, Ladouceur C, McFarland A, Dahl RE, and Ryan ND (2013). Sustained neural alterations in anxious youth performing an attentional bias task: a pupilometry study. Depress. Anxiety 30, 22–30. [PubMed: 22700457]

Reimer J, Froudarakis E, Cadwell CR, Yatsenko D, Denfield GH, and Tolias AS (2014). Pupil fluctuations track fast switching of cortical states during quiet wakefulness. Neuron 84, 355–362. [PubMed: 25374359]

Root CM, Denny CA, Hen R, and Axel R (2014). The participation of cortical amygdala in innate, odour-driven behaviour. Nature 515, 269–273. [PubMed: 25383519]

Schmidt FM, Sander C, Dietz M-E, Nowak C, Schröder T, Mergl R, Schönknecht P, Himmerich H, and Hegerl U (2017). Brain arousal regulation as response predictor for antidepressant therapy in major depression. Sci. Rep 7, 45187. [PubMed: 28345662]

Schneider M, Leuchs L, Czisch M, Sämann PG, and Spoormaker VI (2018). Disentangling reward anticipation with simultaneous pupillometry / fMRI. Neuroimage 178, 11–22. [PubMed: 29733957]

Shin LM, and Liberzon I (2010). The neurocircuitry of fear, stress, and anxiety disorders. Neuropsychopharmacology 35, 169–191. [PubMed: 19625997]

Singewald N, Salchner P, and Sharp T (2003). Induction of c-Fos expression in specific areas of the fear circuitry in rat forebrain by anxiogenic drugs. Biol. Psychiatry 53, 275–283. [PubMed: 12586446]

Sparta DR, Stamatakis AM, Phillips JL, Hovelsø N, van Zessen R, and Stuber GD (2011). Construction of implantable optical fibers for long-term optogenetic manipulation of neural circuits. Nat. Protoc 7, 12–23. [PubMed: 22157972]

Sparta DR, Jennings JH, Ung RL, and Stuber GD (2013). Optogenetic strategies to investigate neural circuitry engaged by stress. Behav. Brain Res 255, 19–25. [PubMed: 23684554]

Stamatakis AM, Sparta DR, Jennings JH, McElligott ZA, Decot H, and Stuber GD (2014). Amygdala and bed nucleus of the stria terminalis circuitry: Implications for addiction-related behaviors. Neuropharmacology 76 (Pt B), 320–328. [PubMed: 23752096]

Straube T, Mentzel H-J, and Miltner WHR (2007). Waiting for spiders: brain activation during anticipatory anxiety in spider phobics. Neuroimage 37, 1427–1436. [PubMed: 17681799]

Stuber GD, and Wise RA (2016). Lateral hypothalamic circuits for feeding and reward. Nat. Neurosci 19, 198–205. [PubMed: 26814589]

Ting JT, Daigle TL, Chen Q, and Feng G (2014). Acute brain slice methods for adult and aging animals: application of targeted patch clamp analysis and optogenetics. Methods Mol. Biol 1183, 221–242. [PubMed: 25023312]

Touriño C, Eban-Rothschild A, and de Lecea L (2013). Optogenetics in psychiatric diseases. Curr. Opin. Neurobiol 23, 430–435. [PubMed: 23642859]

Tovote P, Fadok JP, and Lüthi A (2015). Neuronal circuits for fear and anxiety. Nat. Rev. Neurosci 16, 317–331. [PubMed: 25991441]

Tummeltshammer K, Feldman ECH, and Amso D (2019). Using pupil dilation, eye-blink rate, and the value of mother to investigate reward learning mechanisms in infancy. Dev. Cogn. Neurosci 36, 100608. [PubMed: 30581124]

Urbano FJ, Bisagno V, and Garcia-Rill E (2017). Arousal and drug abuse. Behav. Brain Res 333, 276–281. [PubMed: 28729115]

Walker DL, Miles LA, and Davis M (2009). Selective participation of the bed nucleus of the stria terminalis and CRF in sustained anxiety-like versus phasic fear-like responses. Prog. Neuropsychopharmacol. Biol. Psychiatry 33, 1291–1308. [PubMed: 19595731]

Wilhelm FH, and Roth WT (2001). The somatic symptom paradox in DSM-IV anxiety disorders: suggestions for a clinical focus in psychophysiology. Biol. Psychol 57, 105–140. [PubMed: 11454436]

Author Manuscript Author Manuscript Author Manuscript Author Manuscript

Yassa MA, Hazlett RL, Stark CEL, and Hoehn-Saric R (2012). Functional MRI of the amygdala and bed nucleus of the stria terminalis during conditions of uncertainty in generalized anxiety disorder. J. Psychiatr. Res 46, 1045–1052. [PubMed: 22575329]

Zhou P, Resendez SL, Rodriguez-Romaguera J, Jimenez JC, Neufeld SQ, Giovannucci A, Friedrich J, Pnevmatikakis EA, Stuber GD, Hen R, et al. (2018). Efficient and accurate extraction of in vivo calcium signals from microendoscopic video data. eLife 7, e28728. [PubMed: 29469809]

Author Manuscript
Author Manuscript
Author Manuscript
Author Manuscript

Highlights

- *Prepronociceptin* (*Pnoc*) defines a subpopulation of GABAergic neurons within BNST
- *Pnoc*$^{\mathrm{BNST}}$ neurons encode rapid changes in arousal to motivationally salient stimuli
- Activation of *Pnoc*$^{\mathrm{BNST}}$ neurons drives arousal responses and anxiety-like behavior
- *Pnoc*$^{\mathrm{BNST}}$ neurons exhibit diversity in both anatomical connectivity and genetic identity

Author Manuscript Author Manuscript Author Manuscript Author Manuscript

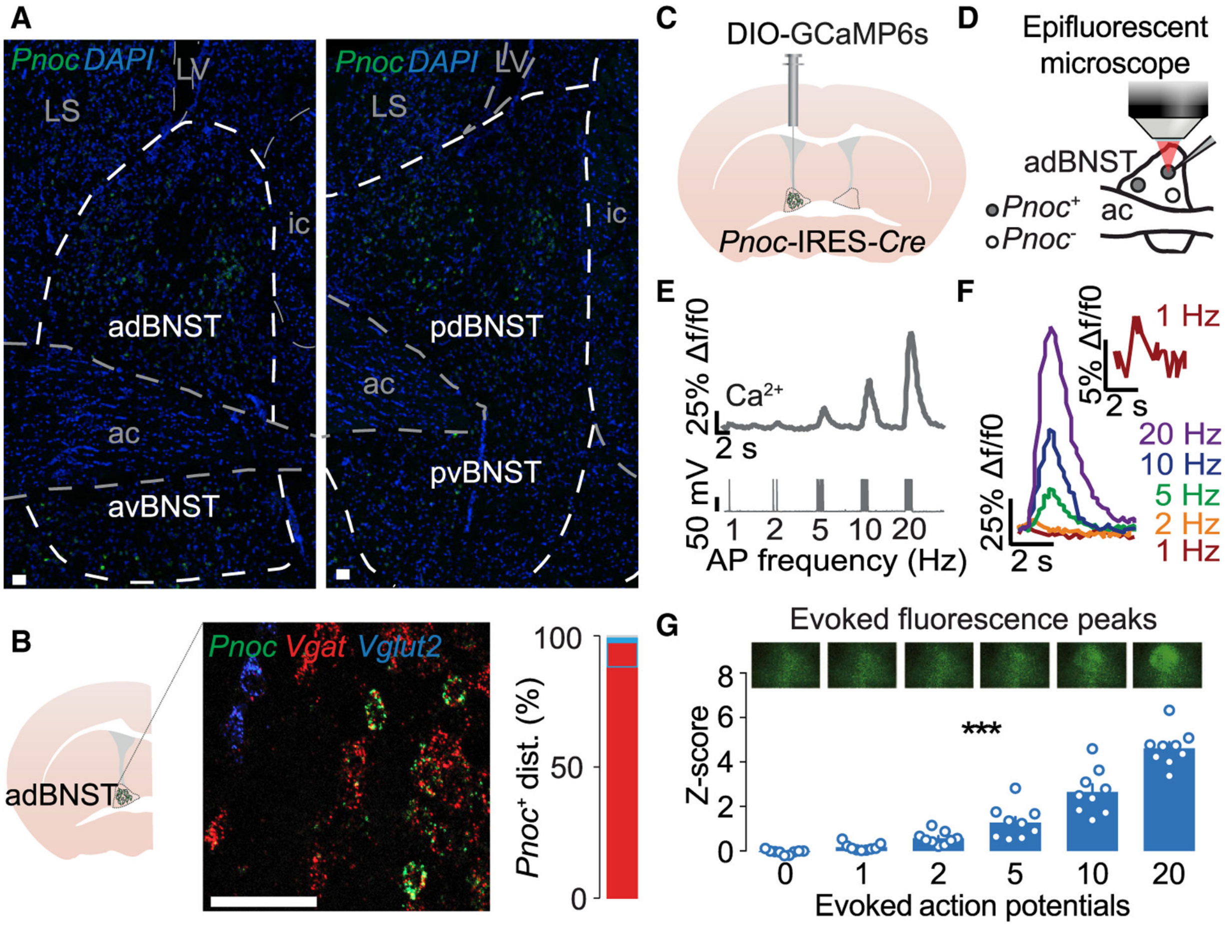

Figure 1. Expression of *Pnoc* Defines a Subpopulation of GABAergic Neurons within adBNST that Can Be Monitored Using Calcium-Imaging Approaches

(A) Confocal images depicting the distribution of *Pnoc*-expressing neurons in BNST using FISH with DAPI counterstain. LV, lateral ventricle; LS, lateral septum; adBNST, anterodorsal BNST; avBNST, anteroventral BNST; pdBNST, posterodorsal BNST; pvBNST, posteroventral BNST; ac, anterior commissure; ic, internal capsule. Scale bars, 40 μm.

(B) Confocal image depicting the overlap between the expression of *Pnoc*, *Vgat*, and *Vglut2* within BNST neurons using FISH (left). Scale bar, 40 μm. Proportion of *Vgat*$^+$ and *Vglut2*$^+$ neurons quantified using FISH (right).

(C) Schematic of injection of AAVdj-EF1α-DIO-GCaMP6s into the adBNST of *Pnoc*-IRES-*Cre* mice.

(D) Schematic of simultaneous patch-clamp electrophysiology and calcium imaging of GCaMP6s-expressing *Pnoc*$^+$ neurons.

(E) Sample traces showing a series of depolarizing pulses (1–20 Hz) applied in current-clamp mode to drive trains of action potentials (bottom), during which GCaMP6s fluorescence was tracked in recorded neurons (top).

(F) Overlay of sample traces showing elevation of GCaMP6s fluorescence signal during the depolarizing pulses, so that a single action potential was detectable (red waveform).

(G) Top: representative images of an individual *Pnoc*^{BNST} neuron showing evoked fluorescence peaks at the various depolarizing pulses. Bottom: action potential generation

Author Manuscript

Author Manuscript

Author Manuscript

Author Manuscript

resulted in linear elevations in GCaMP6s fluorescence (n = 10 neurons). Data are shown as mean ± SEM. ***p < .001.

For a description of statistical analysis and results shown in this figure, please refer to Table S1.

Author Manuscript

Author Manuscript

Author Manuscript

Author Manuscript

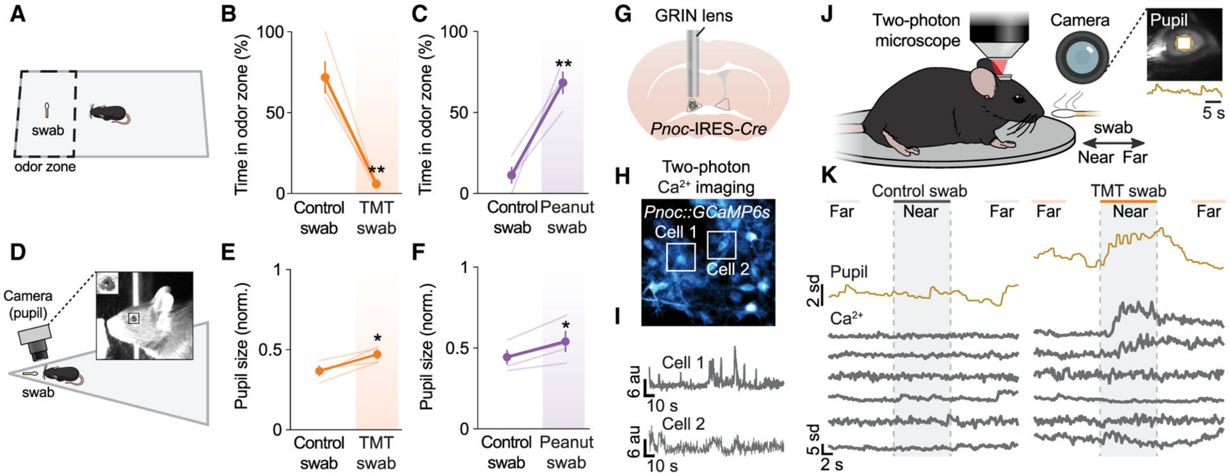

Figure 2. Both Aversive Odor TMT and Rewarding Odor Peanut Oil Increase Physiological Arousal Responses, as Evidenced by Increased Pupillary Size in Both Freely Moving and Head-Fixed Mice Used for Two-Photon Calcium Imaging

(A) Schematic of a freely moving mouse in its home cage to assess avoidance and approach behaviors to a water control, TMT swabs, or peanut oil swabs.

(B) Group average of time in odor zone in mice exposed consecutively to control and TMT swabs (swab was placed in preferred side determined during a baseline before testing; n = 4).

(C) Group average of time in odor zone in mice exposed consecutively to control and peanut swabs (swab was placed in non-preferred side determined during a baseline before testing; n = 4).

(D) Schematic of modified arena used for pupillometry in freely moving animals during exposure to control, TMT, or peanut oil swabs. Image of a mouse sniffing the odor swab. Inset in image shows close-up of the mouse’s pupil.

(E) Group average of normalized pupil diameter between consecutive exposure to control and TMT odor during the first initial contact with the odor swab (n = 4).

(F) Group average of normalized pupil diameter between consecutive exposure to control and peanut odor during the first initial contact with the odor swab (n = 4).

(G) Schematic of implantation of a GRIN lens above adBNST of *Pnoc*-IRES-*Cre* mice injected with AAVdj-EF1α-DIO-GCaMP6s.

(H) Representative image of *Pnoc*$^{\mathrm{BNST}}$ neurons through a GRIN lens.

(I) Extracted calcium traces from two representative *Pnoc*$^{\mathrm{BNST}}$ neurons using CNMF.

(J) Schematic of a head-fixed mouse on a running disc with simultaneous pupillometry under a two-photon microscope while being exposed to a movable odor swab. The odor swab was either 25 cm (far) or 1 cm (near) from the mice. Inset: representative frame of a mouse pupil with size-tracking square and accompanying sample pupil trace.

(K) Sample traces of *Pnoc*$^{\mathrm{BNST}}$ neurons shown based on location of either the control or TMT swab. Data are shown as mean ± SEM. *p < .05; **p < .01.

For a description of statistical analysis and results shown in this figure, please refer to Table S1.

Author Manuscript
Author Manuscript
Author Manuscript
Author Manuscript

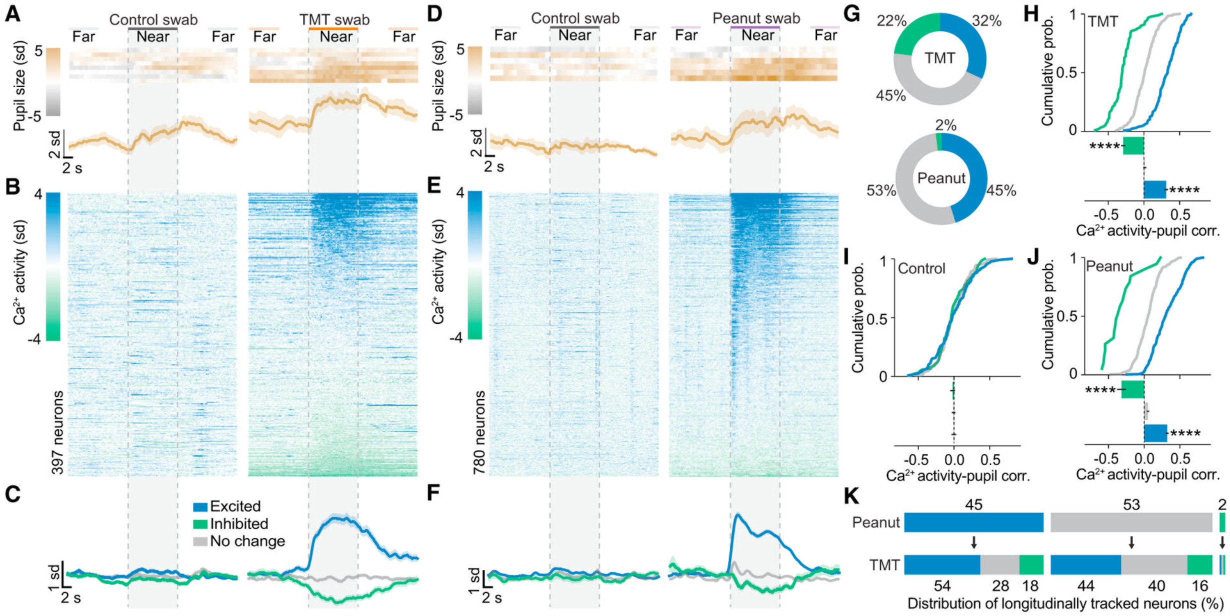

Figure 3. *Pnoc*^{BNST} Neurons Encode Rapid Changes in Arousal to Aversive and Rewarding Stimuli

(A) Heatmap of individual data (top) and average group data (bottom) for pupil responses to control and TMT swabs (n = 4 mice).

(B) Heatmap of responses to the control and TMT swabs from all *Pnoc*^{BNST} neurons, organized by their average response to the TMT swab.

(C) Response dynamics of *Pnoc*^{BNST} neurons to the control and TMT swabs that showed significant excitatory, inhibitory, or no change in activity to the TMT swab (n = 397 neurons).

(D) Heatmap of individual data (top) and average group data (bottom) for pupil responses to control and peanut swabs (n = 3 mice).

(E) Heatmap of responses to the control and peanut swabs from all *Pnoc*^{BNST} neurons, organized by their average response to the peanut swab (n = 780 neurons).

(F) Response dynamics of *Pnoc*^{BNST} neurons to the control and peanut swabs that showed significant excitatory, inhibitory, or no change in activity to the peanut swab.

(G) Top: proportion of excitatory and inhibitory responsive cells when the TMT swab was in the Near (compared to Far) position. Bottom: proportion of excitatory and inhibitory responsive cells when the peanut swab was in the Near (compared to Far) position.

(H) Correlation between Ca^{2+} activity dynamics of single *Pnoc*^{BNST} neurons and pupil size when mice were exposed to the TMT swab (n = 397 neurons).

(I) Correlation between Ca^{2+} activity dynamics of single *Pnoc*^{BNST} neurons and pupil size when mice were exposed to the control swab (excited and inhibited as defined by their response to the TMT swab; n = 397 neurons).

(J) Correlation between Ca^{2+} activity dynamics of single *Pnoc*^{BNST} neurons and pupil size when mice were exposed to the peanut swab (n = 780 neurons).

(K) Neuronal responses to TMT categorized by response to peanut oil. Data are shown as mean ± SEM. ****p < .0001.

Author Manuscript Author Manuscript Author Manuscript Author Manuscript

For a description of statistical analysis and results shown in this figure, please refer to Table S1.

Author Manuscript

Author Manuscript

Author Manuscript

Author Manuscript

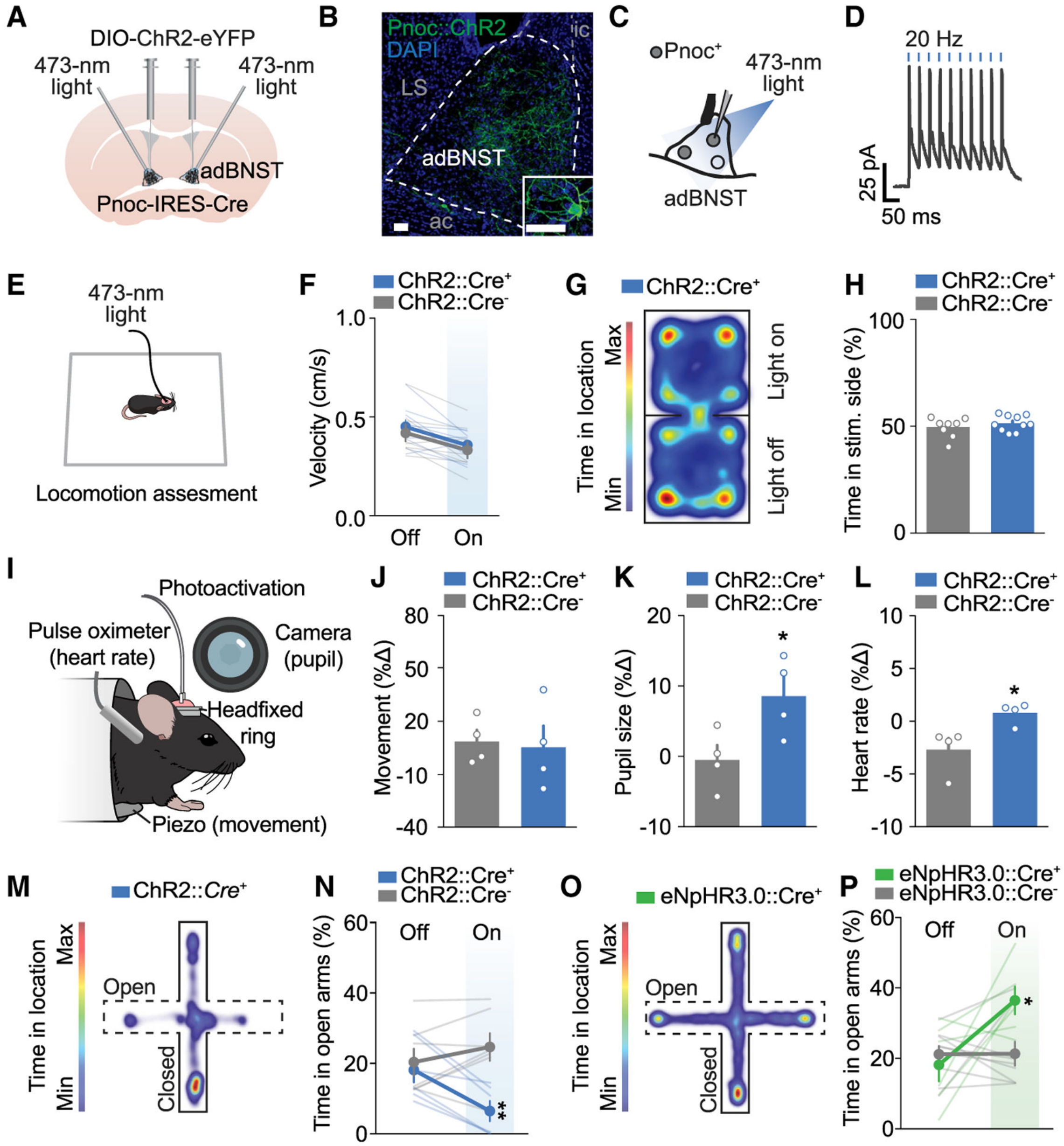

Figure 4. *Pnoc*$^{\text{BNST}}$ Neurons Drive Arousal Responses and Anxiety-like Behavior

(A) Schematic of an injection of AAV5-EF1α-DIO-hChR2(H134R)-eYFP and implantation of fibers into the BNST of a *Pnoc*-IRES-*Cre* mouse.

(B) Confocal image depicting expression of ChR2-eYFP in *Pnoc*$^{\text{BNST}}$ neurons. LS, lateral septum; ic, internal capsule; adBNST, anterodorsal BNST; ac, anterior capsule. Inset: confocal image at high magnification depicting expression of ChR2-eYFP in *Pnoc*$^{\text{BNST}}$ neurons. Scale bars, 40 μm.

(C) Schematic of patch-clamp electrophysiology of ChR2-expressing *Pnoc*$^{+}$ neurons.

(D) Sample neural response of a *Pnoc*$^{\text{BNST}}$ neuron expressing ChR2 in response to blue light at 20 Hz. Group data showed 100% spike fidelity.

Author Manuscript Author Manuscript Author Manuscript Author Manuscript

(E) Schematic of a tethered (for optogenetics) freely moving mouse in an open field arena to assess locomotion.

(F) Group average for velocity with photoactivation of *Pnoc*$^{\text{BNST}}$ neurons (n = 8–9 per group).

(G) Sample heatmap illustrating the location of a mouse during photoactivation of *Pnoc*$^{\text{BNST}}$ neurons during a real-time place preference assay (RTPP).

(H) Group average for time spent in stimulation side during RTPP with photoactivation of *Pnoc*$^{\text{BNST}}$ neurons (n = 8–10 per group).

(I) Schematic of a head-fixed mouse in a cylindrical enclosure with an optical patch cable (photoactivation), a heart rate monitor (pulse oximeter), a movement monitor (piezo sensor), and a camera (pupil).

(J–L) Group average for the change in movement (J; n = 4 per group), heart rate (K; n = 4 per group), and pupil size (L; n = 4 per group) with photoactivation of *Pnoc*$^{\text{BNST}}$ neurons.

(M) Sample heatmap illustrating the location of a mouse during photoactivation of *Pnoc*$^{\text{BNST}}$ neurons during the elevated plus maze (EPM).

(N) Group average for time spent in open arms during EPM with photoactivation of *Pnoc*$^{\text{BNST}}$ neurons (n = 6–7 per group).

(O) Sample heatmap illustrating the location of a mouse during photoinhibition of *Pnoc*$^{\text{BNST}}$ neurons in the EPM using eNpHR3.0-eYFP.

(P) Group average for time spent in open arms during EPM with photoinhibition of *Pnoc*$^{\text{BNST}}$ neurons (n = 6–9 per group). Data are shown as mean ± SEM. $^{*}p < 0.05$; $^{**}p < 0.01$.

For a description of statistical analysis and results shown in this figure, please refer to Table S1.

Author Manuscript

Author Manuscript

Author Manuscript

Author Manuscript

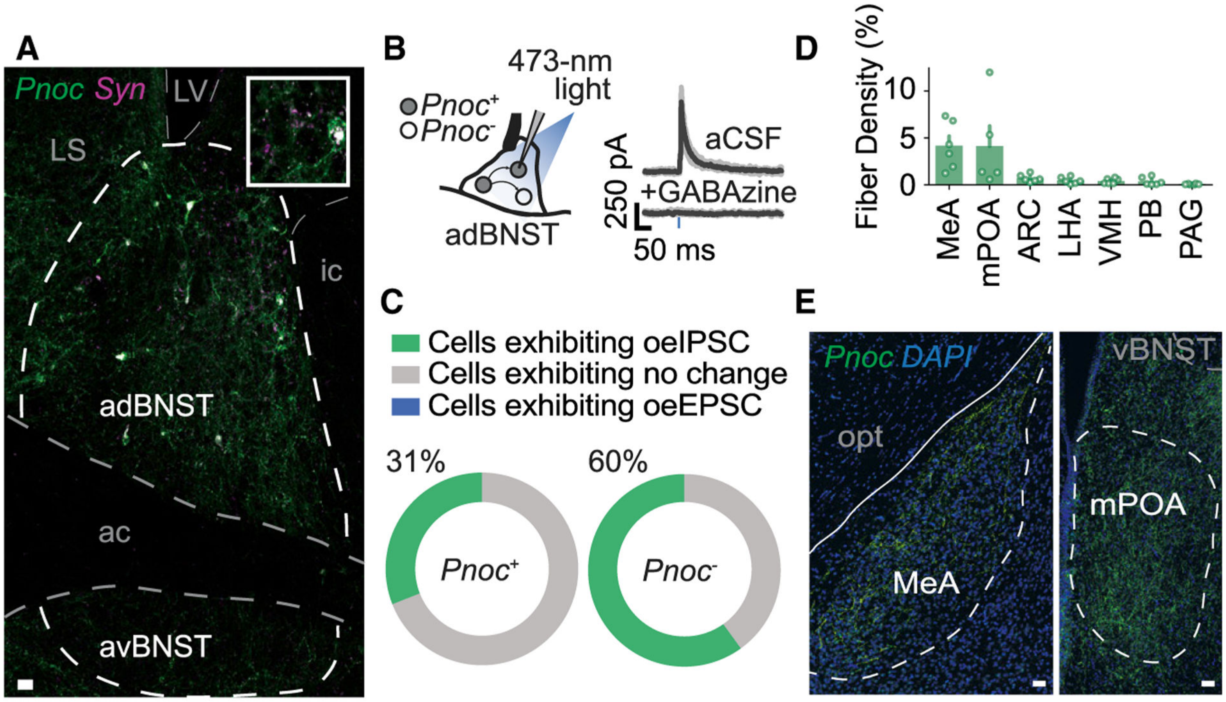

Figure 5. *Pnoc*$^{\text{BNST}}$ Neurons Exhibit Diversity in Anatomical Connectivity

(A) Confocal image depicting the distribution of *Pnoc*$^{\text{BNST}}$ somata and terminals (Syn, synaptophysin-mRuby) after local injection of AAVdj-HSyn-Flex-mGFP-2A-synaptophysin-mRuby. Inset shows higher magnification of the adBNST. LV, lateral ventricle; LS, lateral septum; adBNST, anterodorsal BNST; avBNST, anteroventral BNST; ic, internal capsule; ac, anterior commissure. Scale bar, 40 μm.

(B) Left: schematic of patch-clamp electrophysiology of ChR2-expressing *Pnoc*$^{+}$ neurons. Right: voltage-clamp traces from *Pnoc*$^{\text{BNST}}$ neurons showing optically evoked inhibitory postsynaptic currents (oeIPSCs) being blocked by GABA_{A} receptor antagonist GABAzine (n = 4 neurons). aCSF, artificial cerebral spinal fluid.

(C) Proportion of *Pnoc*$^{-}$ and *Pnoc*$^{+}$ neurons exhibiting oeIPSCs, no change, and optically evoked excitatory postsynaptic currents (oeEPSCs).

(D) Quantification of fiber density (% of area) across distal regions showing fiber labeling in animals expressing ChR2-eYFP in *Pnoc*$^{\text{BNST}}$ neurons (n = 6). MeA, medial amygdala; mPOA, medial preoptic area; ARC, arcuate nucleus; LHA, lateral hypothalamic area; VMH, ventromedial hypothalamus; PB, parabrachial nucleus; PAG, periaqueductal gray.

(E) Confocal image depicting fibers from animals expressing eYFP in *Pnoc*$^{\text{BNST}}$ neurons in the posterodorsal portion of medial amygdala at −1.94 mm from bregma (left) and the medial preoptic area at −0.10 mm from bregma (right). opt, optic tract; vBNST, ventral BNST. Scale bars, 40 μm.

For a description of statistical analysis and results shown in this figure, please refer to Table S1.

Author Manuscript Author Manuscript Author Manuscript Author Manuscript

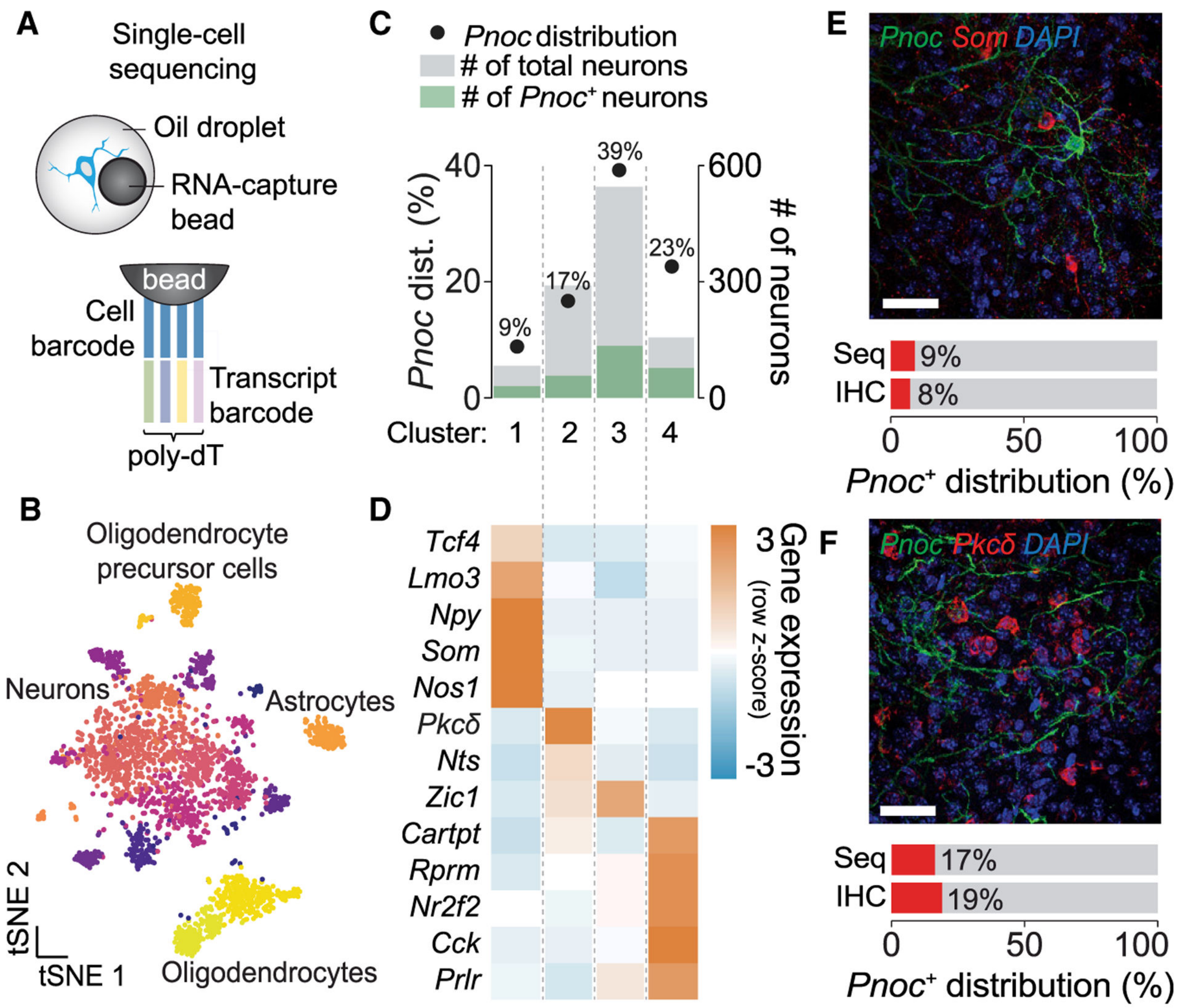

Figure 6. *Pnoc*$^{\mathrm{BNST}}$ Neurons Exhibit Diversity in Genetic Identity

(A) Schematic of the droplet-based method (Drop-seq) used to sequence RNA from thousands of individual cells within BNST (cells, n = 2,492; mice, n = 24).

(B) Gene expression pattern of BNST visualized in tSNE space. Colors represent neuronal clusters.

(C) Distribution of *Pnoc*$^+$ neurons across clusters expressing >5% of *Pnoc*$^+$ cells (left axis). Distribution of the number of total cells and *Pnoc*$^+$ cells across the same clusters (right axis).

(D) Heatmap depicting expression of candidate marker genes for the same neuronal cluster in Figure 4C.

(E) Top: confocal image depicting the overlap between the expression of *Pnoc* and *Som* within BNST neurons using immunohistochemistry. Scale bar, 40 μm. Bottom: distribution of *Som*$^+$ neurons quantified using either Drop-seq (Seq) or immunohistochemistry (IHC).

(F) Top: confocal image depicting the overlap between the expression of *Pnoc* and *Pkcδ* within BNST neurons using immunohistochemistry. Scale bar, 40 μm. Bottom: distribution of *Pkcδ*$^+$ neurons quantified using either Drop-seq (Seq) or immunohistochemistry (IHC).

Author Manuscript
Author Manuscript
Author Manuscript
Author Manuscript

KEY RESOURCES TABLE

REAGENT or RESOURCE	**SOURCE**	**IDENTIFIER**
Antibodies		
chicken anti-GFP (1:1,000)	Aves Labs	cat. no. GFP-1020; RRID: AB_10000240
mouse anti-*PKCδ* (1:500)	BD Biosciences	cat. no. 610398; RRID: AB_397781
rabbit anti-Somatostatin (1:2,000)	BMA Biomedicals	cat. no. T-4103; RRID: AB_518614
donkey anti-Chicken 488 (1:500)	Jackson Immuno Research Labs	cat no. 703-545-155; RRID: AB_2340375
donkey anti-Mouse 647 (1:500)	Jackson Immuno Research Labs	cat no. 715-605-150; RRID: AB_2340862
donkey anti-Rabbit 647 (1:500)	Jackson Immuno Research Labs	cat no. 711-605-152; RRID: AB_2492288
Bacterial and Virus Strains		
AAVdj-hSyn-Flex-mGFP-2A-synaptophysin-mRuby (5.0 × 10^8 infectious units/mL)	Stanford Gene Vector & Virus Core	cat. no. GVVC-AAV-100
AAVdj-EF1α-DIO-GCaMP6s (3.1 × 10^{12} infectious units/mL)	UNC Vector Core	N/A
AAV5-EF1α-DIO-hChR2(H134R)-eYFP (4.3 × 10^{12} infectious units/mL)	UNC Vector Core	N/A
AAV5-EF1α-DIO-eNpHR3.0-eYFP (8.0 × 10^{12} infectious units/mL)	UNC Vector Core	N/A
AAV5-EF1α-DIO-eYFP (6.0 × 10^{12} infectious units/mL)	UNC Vector Core	N/A
Chemicals, Peptides, and Recombinant Proteins		
Mm-*Pnoc* probe	ACDBio	cat. no. 437881
Mm-*Slc32a1* (*Vgat*) probe	ACDBio	cat. no. 319191
Mm-*Slc17a6-C2* (*Vglut2*) probe	ACDBio	cat. no. 319171
Mm-*CaMKIIα*-cust-C2 probe	ACDBio	cat. no. 411851
GABAzine (SR 95531 hydrobromide)	Tocris	cat. no. 1262
2,4,5-Trimethylthiazoline	Forestry Distributing	cat. no. 300000368
Peanut oil	Harris Teeter	N/A
Critical Commercial Assays		
RNAscope Kit	ACDBio	cat. no. 320293
Experimental Models: Organisms/Strains		
prepronociceptin-IRES-Cre mice	This paper	N/A
C57BL/6J mice	Jackson Laboratory	N/A
Software and Algorithms		
ImageJ	NIH	https://imagej.nih.gov/ij
Prism 7	GraphPad	https://www.graphpad.com
Python	Anaconda	https://www.anaconda.com/
Mosaic	Inscopix	https://www.inscopix.com
SIMA v1.3	(Kaifosh et al., 2014)	https://github.com/losonczylab/sima
CNMF	(Zhou et al., 2018)	https://github.com/zhoupc/CNMF_E
Drop-seq data analysis scripts (Python)	This paper	https://github.com/stuberlab
Calcium Imaging data analysis scripts (Python)	This paper	https://github.com/stuberlab

REAGENT or RESOURCE	SOURCE	IDENTIFIER
Deposited Data		
Single cell sequencing data	GEO	accession no. GSE132067

Author Manuscript Author Manuscript Author Manuscript Author Manuscript